1D+1D modeling of reversible Solid Oxide Cell (rSOC) reactors for steady state and dynamic process analyses of electricity storage systems

Master's Thesis

Ruixiao Lin

377526

March 6, 2018

Supervisor: Prof. Dr.-Ing. Matthias Kraume
M.Sc. Srikanth Santhanam

Technische Universität Berlin
Fakultät 3: Prozesswissenschaften
Fachgebiet Verfahrenstechnik

Deutsches Zentrum für Luft- und Raumfahrt
Institut für Technische Thermodynamik
Abteilung Elektrochemische Energietechnik

Thesis declaration/Eidesstattliche Versicherung

I hereby declare, that this master thesis is my own, unaided work and that all sources of information and references being used are listed to the best of my knowledge.

Hiermit erkläre ich, dass ich die vorliegende Arbeit selbstständig und eigenhändig sowie ohne unerlaubte fremde Hilfe und ausschließlich unter Verwendung der aufgeführten Quellen und Hilfsmittel angefertigt habe.

Berlin, 07. Mrz. 2018

_____

(Ruixiao Lin)

Abstract

The intermittent nature of renewable energy sources demands energy storage systems to stabilize the grid. The Reversible solid oxide cell (rSOC) system is a promising solution for energy storage. To facilitate its development, system modeling and simulation is a useful tool. In this work, a 1D+1D transient model of a co/counter-flow planar rSOC stack suitable for system modeling is developed. As a basis, an experimentally validated 1D model of an rSOC single repeat unit (SRU) model is first refined in following aspects: 1. Higher resolution of structures of fuel and air channel is achieved; 2. Better heat convection model between gas flow and solid elements is employed; 3. Dusty gas model (DGM) for multicomponent gas diffusion in porous electrode is implemented; 4. Butler-Volmer equation is adopted instead of its inverse hyperbolic approximation; 5. Electrochemical parameters for calculation of exchange current densities are determined through detailed experimental analysis. Heat transfer between stack and surroundings in the test bench is modeled for validation purposes. The developed stack model is validated against the experimental results.

Acknowledgement

My first thank goes to Mr. Santhanam- my supervisor at DLR- who offered me the possibility to work at DLR and finish my master thesis in this interesting field, for his kind and patient instructions to me and all the nice discussions with him. He also carefully reviewed the different chapters of this thesis. I also want to thank Mr. Riedel for all the kind explanations to my questions about experiment and all the interesting discussions. Dr. Heddrich is also to be acknowledged for his valuable suggestions and good discussions. I really appreciated and enjoyed the working conditions, atmosphere in the group and the opportunity to work in this novel field. Thanks for all that work in the group of High Temperature Systems & Process Development at DLR!

Then, I'd like to thank Mr. Chen for all the enjoyable discussions with him and his kind help during my preparation for my thesis presentation.

Finally, I want to thank Prof. Kraume for the opportunity to finish my thesis at DLR under his supervision and to give my final presentation at Fachgebiet Verfahrenstechinik. Thank also goes to Ms. Herrndorf for her help in thesis registration.

Contents

List of Figures

List of Tables

Nomenclature and Abbreviations

Latin letters:

a	activity coefficient	-
a, b, d	Exponents of partial pressures for exchange current density	-
a_1, a_2, a_3, a_4	coefficients in polynomial equation 4.14	-
A	cross-sectional area	m^2
ASR	area specific resistance	$\Omega \cdot m^2$
B	effective width of air channel	m
c	specific heat capacity	$J/(kg \cdot K)$
d_p	mean pore diameter	m
$D_{\alpha,\beta}$	Binary diffusion coefficient of species α and β	m^2/s
$D_{K,\alpha}$	Knudsen-diffusion coefficient of species α	m^2/s
E	reversible voltage	V
E_a	activation energy	J/mol
FU	fuel utilization rate	-
g	specific Gibbs free energy	J/mol
G	Gibbs free energy	J
h	heat transfer coefficient	$W/(m^2 \cdot K)$
h	specific enthalpy	J/mol
j	current density	A/m^2
j_0	exchange current density	A/m^2
l	length	m
$\dot{m}$	mass flow rate	kg/s
M	molecular weight	g/mol
n	amount of substance	mol
Nu	Nusselt number	-
p	pressure	Pa
Pr	Prandtl number	-
q	charge	C
Q	heat quantity	J
$\dot{Q}$	heat flow rate	W
r	heterogeneous reaction rate	$mol/(m^2 \cdot s)$

r	homogeneous reaction rate	$mol/(m^3 \cdot s)$
R	thermal resistance	K/W
Re	Reynolds number	-
S	entropy	J/K
SU	steam utilization rate	-
t	time	s
tc	tortuosity coefficient	-
T	temperature	K
u	specific internal energy	J/kg
U	internal energy	J
V	volume	m^3
V	actual voltage	V
w	width	m
W_e	electric work	J
x	mole fraction	-
y	mass fraction	-
z	valency number of ions of the substance	-

Greek letters:

α	transfer coefficient	-
γ	prefactor of exchange current density	$A/(m^2 \cdot K)$
ε	porosity	-
ϵ	surface emissivity	-
η	overpotential	V
λ	thermal conductivity	$W/(m \cdot K)$
μ	dynamic viscosity	$kg \cdot m/s^2$
ν	stoichiometric coefficient	-
ρ	density	kg/m^3
σ	electrical conductivity	S/m
τ	thickness	m

Subscripts:

0	standard conditions

act	activation
an	fuel electrode (anode)
AI	air side interconnector
AC	air channel
ca	air electrode (cathode)
$conc$	concentration
el	electrolyte
f	gas flow
FC	fuel channel
FI	fuel side interconnector
in	inlet flow
ohm	ohmic
out	outlet flow
s	solid element

Superscripts:

0	standard conditions
eff	effective value

Abbreviations:

DGM	dusty gas model
EIS	electrochemical impedance spectroscopy
PEN	positive–electrolyte–negative tri-layer structure
rPEMC	reversible polymer electrolyte membrane cell
rSOC	reversible solid oxide cell
SOC	solid oxide cell
SOEC	solid oxide electrolysis cell
SOFC	solid oxide fuel cell
SRU	single repeat unit
SSZ	scandia stabilized zirconia
TPB	triple phase boundary
YSZ	yttria stabilized zirconia

1 Introduction

With the development of renewable energy and distributed power generation, energy storage systems are needed to keep or increase the stability of power grid because of the fluctuation nature of these power generation methods. The energy storage system should be able to store excess electricity as well as produce power at high efficiency. Among many technical routes, “power-to-gas” is one of them with advantages that fuel is easy to be stored for long duration and transported, the storage capacity is large compared to batteries, and that this method can be combined with chemical industry. Electrochemical reactors, in theory, can operate both as a fuel cell and electrolyser. In the fuel cell operation, the electrochemical reactor can generate power with fuel (usually gaseous hydrogen) at high efficiency and are anticipated to be benign in emissions and silent. During electrolysis mode, they can produce chemical energy (hydrogen, syngas etc.) with electricity input. Therefore, the electrochemical reactor technology is a promising candidate for the energy storage system following the “power-to-gas” route.

There are six types of electrochemical reactors, usually named according to the types of electrolyte. Two of the six types are mainly studied for their application in energy storage: reversible polymer electrolyte membrane cells (rPEMC) and reversible solid oxide cells (rSOC).

Strong development efforts are made for rPEMC technology. rPEMC operates at low temperature (between ambient and 100℃): producing hydrogen or generating electricity with hydrogen and is very sensitive to its quality. This means, electricity has to be stored in the form of hydrogen. Water management in the membrane is another key issue.

rSOC operates at high temperature (between 550℃ and 1000℃). High temperature brings several advantages: power generation is possible with hydrogen, carbon monoxide and hydrocarbon fuels with or without prior reforming, which means electricity can also be stored as liquid hydrocarbon fuels; power and high grade heat (even cold) can be co-generated; water and carbon dioxide can be co-electrolyzed; it has the potential to reach a competitive cost as no expensive catalyst is necessary. The electrolyte is a solid dense oxide, so water management is not an issue for rSOC. High temperature can also result in some problems, such as high thermal stress or requirement of employing ceramics which has manufacturing difficulty. Use of rSOC in an energy storage system is studied and developed in German Aerospace Center. Modeling and simulation is a useful tool to study and understand behavior of rSOC sys-

tems, where electrochemistry, chemistry, fluid mechanics, mass, heat and charge transfer phenomena combined and simulation can provide valuable insight.

This thesis considers the modeling of a co/counter-flow planar rSOC stack for steady state and dynamic process analyses of electricity storage systems. An experimentally validated 1D model of an rSOC single repeat unit (SRU), which is a discretization unit of a single cell, is available in house and should be first refined and then expanded into 1D+1D multi cell rSOC stack model. Final stack model should be modular, computational efficient and compatible for process system modeling. The stack model will be validated against the experimental results available at German Aerospace Center. Before validation, the heat transfer conditions between stack and surroundings in the test bench should also be modeled. The main contribution of this work is to develop for the first time (to the author's knowledge) a 1D+1D rSOC stack model which is suitable for applying in system modeling. In this thesis, the stack model as well as modeling of heat transfer between stack and surroundings will be described in detail, key characteristics of the model and validation results will be shown.

2 The reversible solid oxide cell

2.1 Operating principle

A reversible solid oxide cell (rSOC) can function as a device in the power grid for load shifting. It operates in fuel cell mode converting directly the chemical energy of a (stored) fuel (usually hydrogen or syngas) into electricity when demand exceeds supply, and works in electrolysis cell mode storing excess electricity by converting water and/or carbon dioxide to produce storable fuel. The overall chemical reactions which take place in the rSOC reactors are the same as combustion reactions (in fuel cell mode) or their reverse reactions (in electrolysis mode) (see equation 2.1 and 2.2).

$$H_2 + 0.5O_2 \leftrightarrow H_2O \tag{2.1}$$

$$CO + 0.5O_2 \leftrightarrow CO_2 \tag{2.2}$$

Although the overall reactions are the same, the processes of actual reactions in the fuel cell and in combustion equipment are quite different. One of the essential differences is that the electron transfer during the combustion happens on the subatomic scale so that the transformed energy can only be harvested in the form of heat, while the electron transfer in a fuel cell happens on a much larger scale through the external circuitry so that the chemical energy can be directly converted to electric energy, which means there is no limit of the Carnot cycle and high efficiency can be achieved. The key to realize reconstruction of chemical bonds on large scale is dividing an overall reaction into two half reactions which take place at fuel electrode (see equation 2.3 and 2.4) and air electrode (see equation 2.5) respectively. These half reactions are so called electrochemical reactions.

$$H_2 + O^{2-} \leftrightarrow H_2O + 2e^- \tag{2.3}$$

$$CO + O^{2-} \leftrightarrow CO_2 + 2e^- \tag{2.4}$$

$$0.5O_2 + 2e^- \leftrightarrow O^{2-} \tag{2.5}$$

The two electrodes are separated by an electrolyte which conducts oxygen ions and is electron insulator (see figure 2.1). The electrodes and electrolyte are core components for the electrochemical reactions in the rSOC. Besides, interconnector is also an indispensable component. Figure 2.2 shows the main components of an SOC, details of which are given in the following.

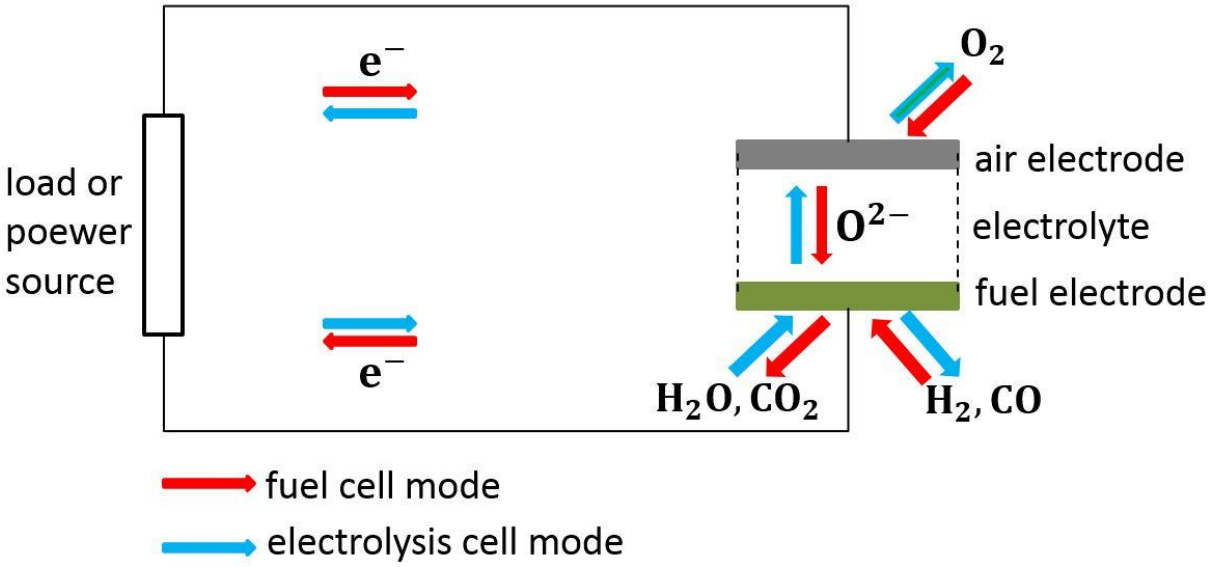

Figure 2.1: Principle of an rSOC

Electrolyte: The electrolyte of rSOC is a solid oxide ceramic material possessing sufficiently high ionic conductivity and low electronic conductivity at the cell operating temperature. It must be stable in both reducing and oxidizing environment and high temperature (600-1000℃). The most common electrolyte used now is yttria stabilized zirconia (YSZ), with the amount of yttrium doping ranging from 3% to 12% molar (Larrain [2005]). An alternative to YSZ is the scandia stabilized zirconia (SSZ), which has higher ionic conductivity but worse anti-degradation performance at high temperature (Uchida et al. [1998] and Yamamoto et al. [1995]). Therefore, YSZ performs well at high temperature (800-1000℃) while SSZ is attractive especially for intermediate temperature (600-800℃). Except for the zirconia-based oxide ion conductors the ceria-based oxide ion conductors are also suggested as an alternative electrolyte especially for low temperature (550-600℃) SOC (Takahashi [1989]). Thickness of the electrolyte depends on the design of the cell. There are now two mainstream cell designs concerning the mechanical support of the cell: anode-supported and electrolyte-supported. For the anode-supported cell, electrolyte is generally 5 to 20μm thick. For the electrolyte-supported cell, typical thickness of the electrolyte is around 90μm (Larrain [2005]).

Fuel electrode (anode): The fuel side electrode must possess these three properties: 1. It should be porous so that the reactant-gas can transfer from the bulk flow zone to the triple phase boundary (TPB) (see figure 2.3) of gas, electrode and electrolyte where the electrochemical reactions happen; 2. It is catalytic for fuel oxidation; 3. It has high electrical conductivity. To fulfill these basic requirements, porous cermet (a fine mixture of ceramic and metal

grains) is usually chosen as the electrode material. Porous cermet of nickel and YSZ (Ni/YSZ) has been until now the most successful, although it does exhibit problems such as carbon fouling from carbonaceous fuels (Singhal and Kendall [2003]). Nickel produces good catalytic activity and electrical conductivity. The electrolyte YSZ particles are first recognized by Spacil [1970] that the mixing of them with nickel matrix can solve the nickel aggregation problem at high temperature. Besides, this mixing has an additional effect: It means the spread of ion-conducting electrolyte into the electrode, which enlarges the area of TPB and so benefits the reaction rate (see figure 2.3). Some other kinds of porous cermet are also applied or under study which show more excellent performance. Riegraf et al. [2017] for example research the SOFC with nickel/gadolinium-doped ceria (Ni/CGO) based fuel electrode, which shows a significantly higher sulfur tolerance than Ni/YSZ. The thickness of fuel electrode for an anode-supported cell is in usually in the range of 200μm to 2mm, while that for an electrolyte-supported cell ranges in general from 20 to 50μm.

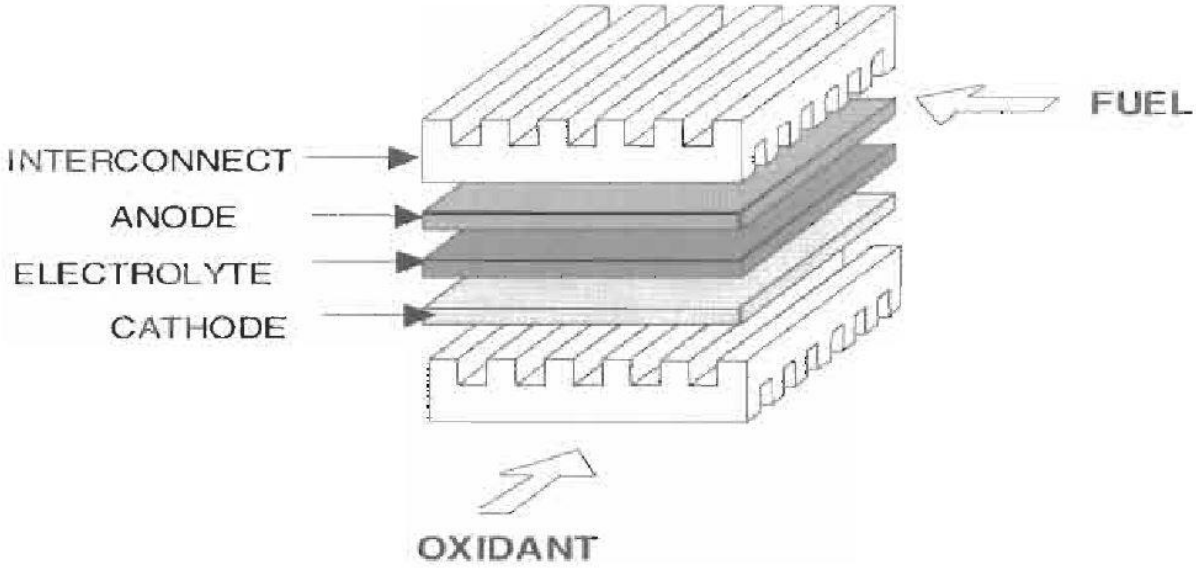

Figure 2.2: Main components of an SOC (Singhal and Kendall [2003])

Air electrode (cathode): Like the fuel side electrode, the air side electrode must also be porous and combine high electrical conductivity with high catalytic activity for oxygen reduction. The requirement to the catalytic activity is different for air electrode and fuel electrode, so the material chosen also differs. Nowadays, the air electrode is mostly composed of a porous perovskite material, which is a relatively good electron conductor at high temperature in oxidizing atmosphere. Representatively applied are strontium doped lanthanum manganite (LSM), strontium doped lanthanum cobaltite (LSC) and strontium doped lanthanum ferrite

(LSF). Besides, material doped with more than one element, e. g. strontium and cobalt doped lanthanum ferrite (LSCF), has also been investigated (Bae and Steele [1998]). Similar to the fuel electrode, the electrolyte material YSZ is usually mixed with the perovskite to increase the reaction area at the TPB (see figure 2.3). The thickness of air electrode is generally around $30\mu m$.

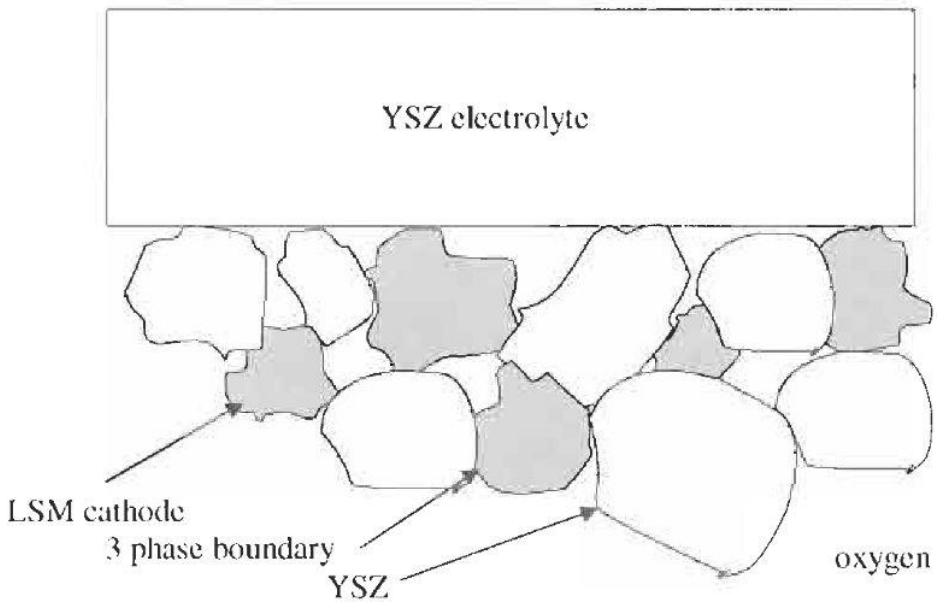

Figure 2.3: Concept of extended triple phase boundary (Singhal and Kendall [2003])

Interconnector: The three main functions of interconnector are: electrical connection between cells, separation of fuel and air and to form the gas flow channel together with the electrode. As figure 2.2 shown, interconnector is the positive pole of a cell as well as a negative pole of the adjacent cell, so interconnector is also called bipolar plate. The interconnector should meet at least the following properties: high electronic conductivity, low ionic conductivity, stability with respect to both oxidizing and reducing environment at high temperature, thermal expansion match to other parts. These high requirements constrain the selection of material. Two kinds of material are commonly used: perovskite-type oxide ceramics based on rare earth chromite or metallic alloys. The former one is for high-temperature (900-1000℃) SOC, expensive and relatively difficult to fabricate; while the latter is suitable for intermediate-temperature (600-850℃) SOC, less costly and easier to fabricate (Singhal and Kendall [2003]).

Besides the structure, it is also necessary to understand briefly the theory on the ability of SOC to convert chemical energy to electrical energy and the reverse. This ability is mainly determined by thermodynamics, kinetics, charge transfer and mass transfer.

Thermodynamics determines the limit of voltage (also called reversible voltage) produced or consumed by an SOC. For the fuel cell mode it is the upper limit. For the electrolysis mode it is the lower limit. From the first and second law of thermodynamics (equation 2.6 and 2.7), relation between the electric work and the Gibbs free energy can be obtained (equation 2.8).

$$dU = \delta Q - (\delta W_e + pdV) \tag{2.6}$$

$$dS \geq \frac{\delta Q}{T} \tag{2.7}$$

$$W_e \leq -\Delta G \tag{2.8}$$

The last equation above, combined with the relation between electric work and electric potential (equation 2.9) and the Faraday's law of electrolysis (equation 2.10), constitutes the "bridge" between thermodynamics and electrochemistry (equation 2.11).

$$W_e = Eq \tag{2.9}$$

$$q = nzF \tag{2.10}$$

$$E \leq \frac{-\Delta G}{nzF} \tag{2.11}$$

The Gibbs free energy is a function of temperature, pressure and component fraction. Databanks, tables or correlations for the Gibbs free energy of pure substance under standard pressure and at different temperatures are usually available, which means that the reversible voltage under standard pressure and without the consideration of the impact of substances mixing is also available. To calculate the reversible voltage under non-standard pressure as well as taking into account the effect of mixing, the Nernst equation plays an important role (equation 2.12).

$$E = E^0 - \frac{RT}{zF} \ln \frac{\prod a_{i,products}^{\nu_i}}{\prod a_{i,reactants}^{-\nu_i}} \tag{2.12}$$

The thermodynamic activity a is a measure of the "effective concentration" of a species in a mixture. For ideal gas, $a_i = p_i/p_0$.

Kinetics determines the loss due to the irreversibility of electrochemical reactions. The reversible voltage can exist only when the reactions are in equilibrium, i.e. the SOC is in open circuit. To overcome the energy barrier and produce electric current, additional electrical potential (called activation overpotential) is the price that needs to be paid. The famous Butler-Volmer equation describes the relation between the electric current density and the activation overpotential (equation 2.13).

$$j = j_0(e^{\alpha z F \eta_{act}/RT} - e^{-(1-\alpha) z F \eta_{act}/RT}) \tag{2.13}$$

Charge transfer causes the irreversible loss called the ohmic overpotential η_{ohm}, which is determined by the total resistance of the circuit and follows the Ohm's law. There exist two kinds of charge transfer in an SOC: the flow of electrons through the electrodes, interconnector and their interfaces, and the flow of ions through the electrolyte. The latter is the main contributor to the total resistance. For example, the ionic resistivity of YSZ at 800℃ is ca. $50\Omega \cdot cm$, while the electronic resistivity of LSM is about $10^{-2}\Omega \cdot cm$ and that of Ni/YSZ is on the order of $10^{-4}\Omega \cdot cm$ (Singhal and Kendall [2003]). Thus, the contribution of the electrolyte to the ohmic overpotential can be very dominant, especially for electrolyte-supported cells. It is worth noting that the resistivity of material is temperature dependent.

Mass transfer leads to the irreversible loss named the concentration overpotential η_{conc}. Concentration difference is needed to drive the mass transfer of reactants from bulk flow to the TPB and products from TPB to bulk flow through the porous electrodes. This means that the concentrations of reactants are lower and that of products are higher at the TPB than in the bulk flow, which gives rise to the decrease (for fuel cell mode) or increase (for electrolysis cell mode) of voltage according to the Nernst equation.

Actual voltage of an SOC is calculated with equation 2.14. For fuel cell, all three overpotentials are positive, so the actual voltage is lower than reversible voltage. For electrolysis cell, all three overpotentials are negative, so the actual voltage is higher than reversible voltage.

$$V = E - \eta_{act} - \eta_{ohm} - \eta_{conc} \tag{2.14}$$

All the three overpotentials are strongly related to the current density. Therefore, the V-j curve is widely employed to show the overall characteristic of an SOC. Figure 2.4 demonstrates a typical V-j curve of an SOC in both fuel cell and electrolysis cell mode.

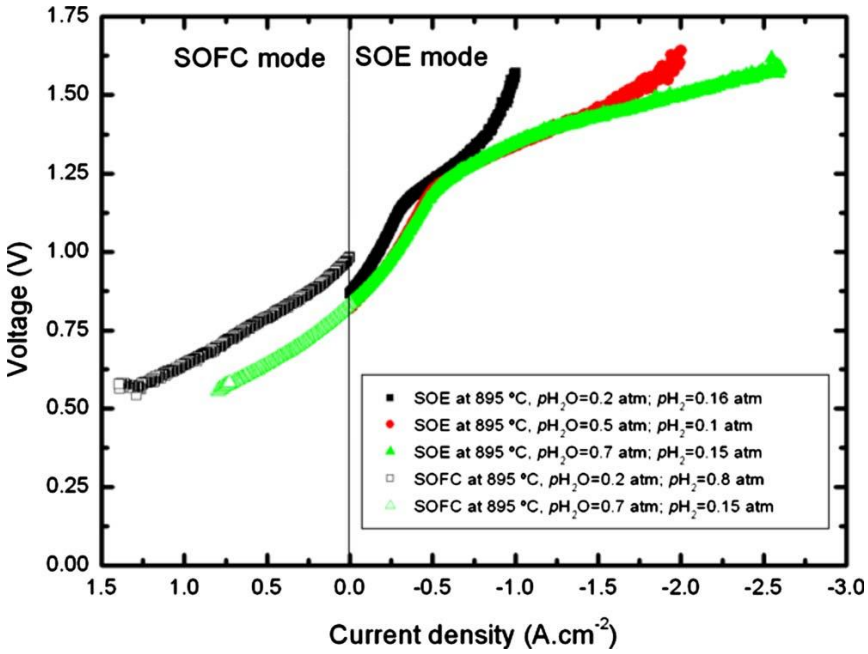

Figure 2.4: Typical V-j curves of an SOC in electrolysis and fuel cell mode (Laguna-Bercero et al. [2010])

2.2 From cell to stack

It can be seen from figure 2.4 that the voltage of a single cell is relatively low (ca. 1V) and power density is limited. Besides, the surface of a single cell is usually restricted to the order of $100cm^2$ because of the fabrication technique. Thus, cells are assembled in series to obtain higher voltage and in parallel to achieve larger current. Both ways of stack assembling can realize a higher power. Two main configurations are currently developed: tubular stack and planar stack. Figure 2.5 illustrates a tubular SOC, advantage of which is easier sealing. However, it is more expensive and with lower power density. Figure 2.2 displays a planar SOC. The present work considers a planar stack, which is formed by series-assembling of cells (see figure 2.6). Inlet gas flow is almost evenly distributed and exit flow is collected by manifolds.

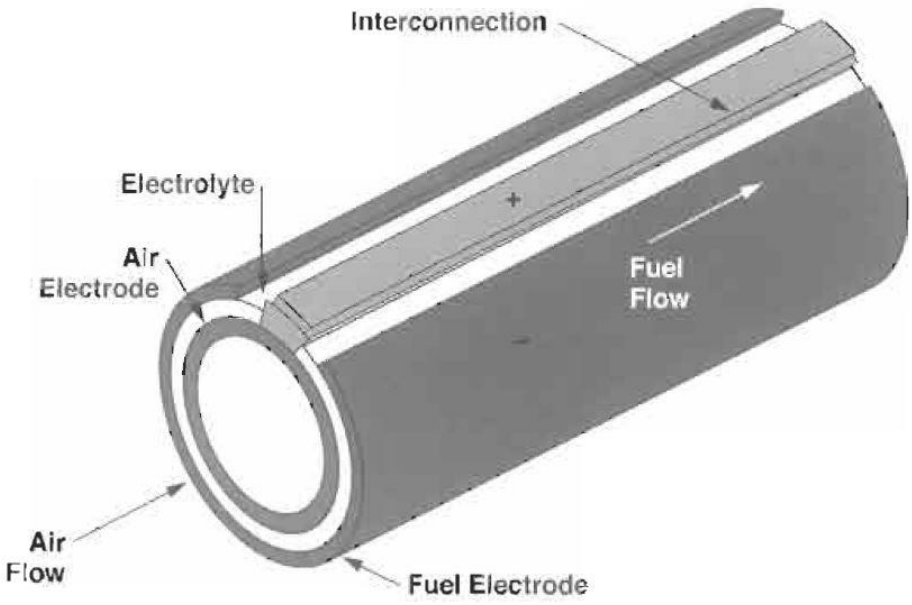

Figure 2.5: Schematic illustration of a Siemens Westinghouse tubular SOC (Singhal [2000])

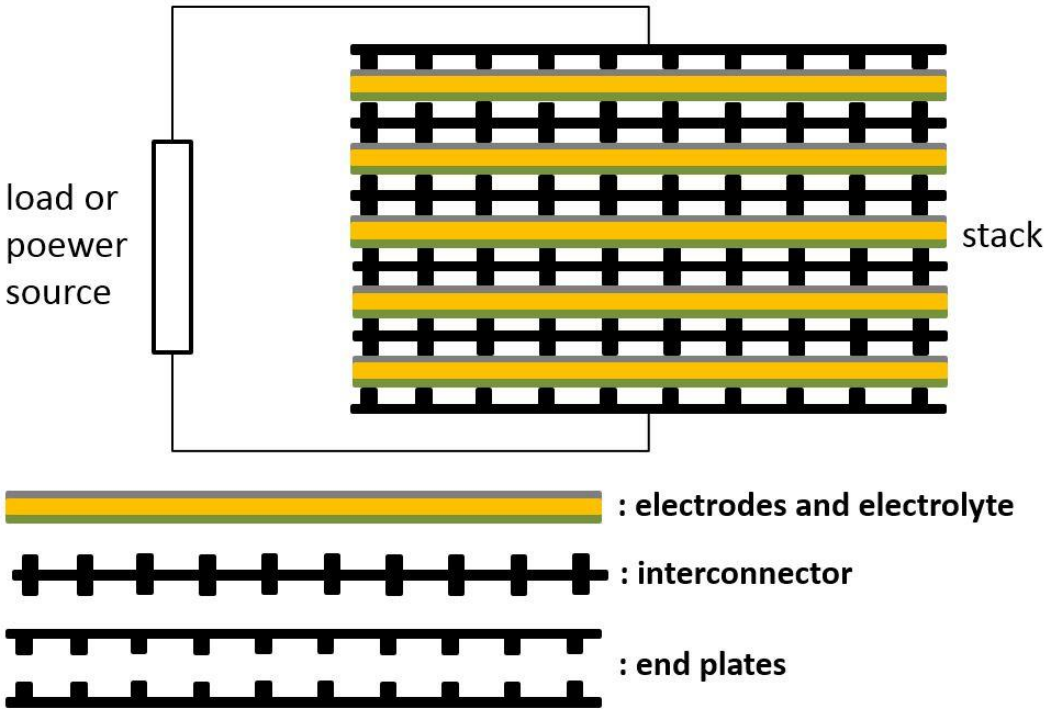

Figure 2.6: Schematic diagram of a planar stack

3 Literature review

There have been many published models for solid oxide cells (SOCs), which range from the basic phenomena at the triple phase boundary (TPB) of the electrolyte, electrode and gas to single repeat unit (SRU), cells, stacks and systems. In this work, the models for SRU, cells and stacks are hierarchically built, so the focus of the literature review is on these kinds of models. Such models can be for different geometries (tubular or planar), PEN structures (anode-supported or electrolyte-supported) and flow configurations (cross-, co- or counter-flow). Most of the papers reviewed here are for the planar geometry, because the object of this modelling project is a planar stack. Besides, the planar design draws more researchers' attention in recent years than the tubular one because of the high energy densities and efficiencies as well as low fabrication costs yielded by such design.

The models can be classified according to their different complexities. One of the main aspects of the model complexity is the dimension. Range of the published models goes from zero to three-dimensional. The most important factor for the model developers to decide the dimension is the purposes of the modelling.

0-D model or block model is like a "black box", which calculates the outputs from system inputs, while the variables inside are not interested. This kind of model is often used in system-level modelling, where the SOCs stack is only a block in the whole system and the goals are exploring system dynamic and design of controllers (Doherty et al. [2010] and Doherty et al. [2015]). System model made of many sub-models is complex, so the stack sub-model usually stays simple to not burden the CPU. 0-D models can also be developed if the aim is to explore only the electrochemical characteristics or to represent a very small single cell (Leonide et al. [2009]).

1-D model considers the discretization along the gas flow direction (co- or counter-flow). For SRU or cells this sort of model is favorable when the flow configuration is simple so that the transfer phenomena along the coordinate axis which is perpendicular to the height and the gas flow direction is negligible and when the detailed fluid dynamics is not of an interest (Aguiar et al. [2004] and Klotz et al. [2014]).

In the overwhelming majority of the modelling works, stack model is hierarchically built based on the single repeat unit and cell. There exist two ways for the hierarchical construction

of stack model: 1. Assuming that all cells in a stack perform exactly same so that the single cell model can already stand for the whole stack; 2. Connecting the single repeat unit or cell model to form a stack model so that the interacts between adjacent cells and other associated influences are included.

If the first way is adopted to construct a stack model from 1-D single cell model, then the 1-D stack model is obtained. Such stack model is usually for simulations of integrated systems (Salogni and Colonna [2010] and Sorrentino et al. [2008]).

2-D SRU or cell model considers the discretization along the gas flow direction and the direction perpendicular to it and to the height. Two dimensions are needed when the flow configuration is complex (e.g. cross-flow) or the detailed fluid dynamics such as the influence of the flow channel geometry on the operation of the fuel cell are centered in the research task (García-Camprubí et al. [2014] and Jin and Xue [2010]). Such models play an important role in assisting the design and optimization and understanding the behaviors of SOCs (Menon et al. [2015] and Laurencin et al. [2011]).

3-D SRU or cell model is rarely seen. The reason is that the height of a single cell is very small and changes along this direction can be neglected. If the second way of constructing a stack model from a 2-D SRU or cell model is employed, then the 3-D stack model is achieved. Such models are too complex to be implemented in system-level modelling. Instead, purpose of this kind of model is to understand the behaviors of a complete stack, e. g. the influence of the heat loss through end plates (Achenbach [1994], Larrain [2005] and Roos et al. [2003]).

There are also other aspects of model complexity, which is determined by the researcher considering the objective of the study and computing power. The pressure drop along the gas flow direction is very small and is not a matter of interest in some studies, so that a constant pressure in the cell or stack is assumed (Sorrentino et al. [2008] and Aguiar et al. [2004]). Some researchers consider the simultaneous electrochemical conversion of H_2 and CO (Achenbach [1994], Roos et al. [2003] and Menon et al. [2015]), while most of the studies consider the conversion of H_2 as the only electrochemical reaction, because the conversion of CO through the water-gas shift is thought to be much faster. Larrain et al. [2003] focuses on the sensitivity of thermal gradient to thermal properties of the materials, therefore the kinetic model is kept simple with an overall resistance responsible for all kinds of overpotential. On

the contrary, some researchers focus not on the thermal properties but the electrochemical characters, and the isothermal assumption is made (Klotz et al. [2014] and Menon et al. [2015]). Imperfect behavior of the electrolyte in included in Larrain [2005], which means the electrolyte is considered to be able to conduct electrons as well, while in most of the studies the electrolyte is assumed as a perfect insulator for electrons. Some do not explore the effect of internal methane-steam reforming (Leonide et al. [2009] and Klotz et al. [2014]), while others consider it (Aguiar et al. [2004] and Salogni and Colonna [2010]). Larrain et al. [2006] uses Wagner´s law for oxide scale grow which causes interconnector degradation and correlates the anode reoxidation potential to the oxygen partial pressure on the anode, to explain the degradation process. To describe the gas diffusion into the porous electrode, many researchers apply the simple Fick´s law for binary system or extended Fick´s law which takes into account the Knudsen diffusion, but there are still some who use more complex dusty gas model (DGM) which describe the multi-component gas diffusion in porous media (García-Camprubí et al. [2014] and Menon et al. [2015]) or its analytical solution (Laurencin et al. [2011]). Computer hardware technology develops very fast, so more compromises because of the limit of computing power can be found in earlier studies. Karoliussen et al. [1998] for example defines effective electric and thermal conductivities for the repeating unit cell elements to achieve a significant degree of simplification.

Modelling work is realized with the help of a software or modelling environment. The commonly utilized modelling environments for SOCs can be categorized into four groups: CFD software, software for simulation of chemical engineering process, causal approach and a-causal approach. CFD software such as OpenFOAM is used to implement detailed CFD model, whose attention is paid on the details of physical fields inside a cell or stack (García-Camprubí et al. [2014] and Jin and Xue [2010]). Software for simulation of chemical engineering process such as Aspen Plus is expert in dealing with balance of plant and plays an important role in the modelling of a SOCs system. Drawback of this kind of software in SOCs modelling is that it is not specialized in electricity and electrochemistry. For example, the half-reactions and the transportation of oxygen ions cannot be modelled in Aspen Plus, so the overall reaction is used (Doherty et al. [2010] and Doherty et al. [2015]).

Causal approach and a-causal approach are two fundamentally different ways of structuring modular models, i.e., the model of a complex object is obtained by connection of its components (Casella et al. [2007] and Casella and Colonna [2012]). In causal or so called block-

oriented approach, modularity is achieved by representing each model-component with a computational block, which represents the model equations in the state-space form. The interface of each module is defined in terms of input and output variables. By following commonly used rules, no algebraic loops can occur, and standard ordinary differential equation (ODE) solvers can be used for simulation. Typical software of this kind is Matlab/Simulink. In a-causal or so called object-oriented approach, each component equations system does not need to be manipulated into a state-space form and the interface of each module is defined by physical ports which introduce new equations describing the relation between variables at each boundary without pre-defined causality. The resulting equations system is usually a very large differential algebraic system of equations (DAE), which means more powerful solvers are needed. Typical software of this kind is gPROMS, and Modelica is a programming language adopting this kind of approach.

Before running the simulation, many parameters need to be entered into the model, among which the electrochemical parameters (e.g. transfer coefficient in the B-V equation) are very important. Many researchers however take these important parameters directly from literature (Aguiar et al. [2004], Larrain [2005], Doherty et al. [2010], Salogni and Colonna [2010] and Laurencin et al. [2011]) or determine them by simple fitting (Xie and Xue [2012] and Grondin et al. [2011]). Such methods are not so appropriate because many factors such as geometry, micro structure and materials would influence the parameters and different cells and stacks should have different parameters. The impedance spectroscopy is a proper way to distinguish different electrochemical processes in SOCs, so that the electrochemical parameters can be more accurately calculated. Only few modelers adopt this way. Leonide et al. [2009] identifies the electrochemical parameters by means of impedance spectroscopy for a 0-D single cell model.

Only in recent years the use of SOCs in energy storage systems (so called reversible solid oxide cell (rSOC)), which produce hydrogen with excess electricity and produce power with hydrogen when demand exceeds supply, draws more and more attention. So, there are more models for solid oxide fuel cells (SOFCs), less models for solid oxide electrolysis cells (SOECs) and only few for rSOC. Besides, the models can also be grouped into steady-state and dynamic. Table 3.1 summarizes the different ways of classification.

Table 3.1: Classification of the models in literature and model developed in this work

	Steady-state			Dynamic		
	SOFC	SOEC	rSOC	SOFC	SOEC	rSOC
SRU or cell model						
0-D	Leonide et al. [2009]					
1-D	Sorrentino et al. [2008]		Klotz et al. [2014]	Aguiar et al. [2004], Salogni and Colonna [2010]		
2-D	Roos et al. [2003]	Laurencin et al. [2011]	García-Camprubí et al. [2014]	Achenbach [1994], Larrain [2005], Larrain et al. [2006]	Menon et al. [2015]	Jin and Xue [2010]
Stack model						
0-D	Doherty et al. [2010], Doherty et al. [2015]					
1-D	Sorrentino et al. [2008]			Salogni and Colonna [2010]		
2-D						Model developed in this work
3-D	Larrain et al. [2003], Roos et al. [2003]			Achenbach [1994], Larrain [2005], Larrain et al. [2006]		

Table 3.1 also shows the scientific gap between the existed models and the model developed in this work: There are no dynamic 2-D stack models for rSOC whose aim is to be used in system-level modelling and which is hierarchically built from a dynamic 1-D SRU model. Furthermore, the identification of the electrochemical parameters by electrochemical imped-

ance spectroscopy experiments with the stack and the implementation of the analytical solution of DGM for describing the multi-component gas diffusion in the porous electrode highlight the specialty of this model. The Modelica language is adopted for this modelling task, which is an a-causal approach, because it is not necessary to develop different models of the same physical object, whose only difference is the causality of the input-output variables (Casella et al. [2007]), which is the situation for the SOFC and SOEC mode of an rSOC.

4 Models for a reversible solid oxide cell stack

In the present work, a 1D+1D non-linear dynamic model of an rSOC stack suitable for integration into models of complex power plants is developed. The modelling object is the co-flow planar stack from sunfire GmbH consists of 10 cells which are electrolyte-supported. Table 4.1 shows some basic geometry parameters of the stack. Model is implemented using the Modelica language under the commercial environment Dymola, which allows for a high degree of flexibility and modularity. Moreover, the Modelica language is naturally suitable for modelling an rSOC, which includes both SOFC mode and SOEC mode in the same model, due to its acausal character. It is very easy to switch between SOFC and SOEC mode with this model. Besides different inlet gas compositions, the only change that should be noted between these two modes is that the value of electric current is positive for SOFC mode and negative for SOEC mode. The developed model can also simulate the counter-flow stack and the stack composed of arbitrary number of cells. Figure 4.1 illustrates the structure of the stack that is used in the laboratory bench for this work. In this thesis, the x axis is the gas flow direction. The red dashed line marks the boundary of the effective reactive area of the stack where the chemical and electrochemical reactions take place. It should be noted that the red dash line also shows the boundary of the stack model developed in this work.

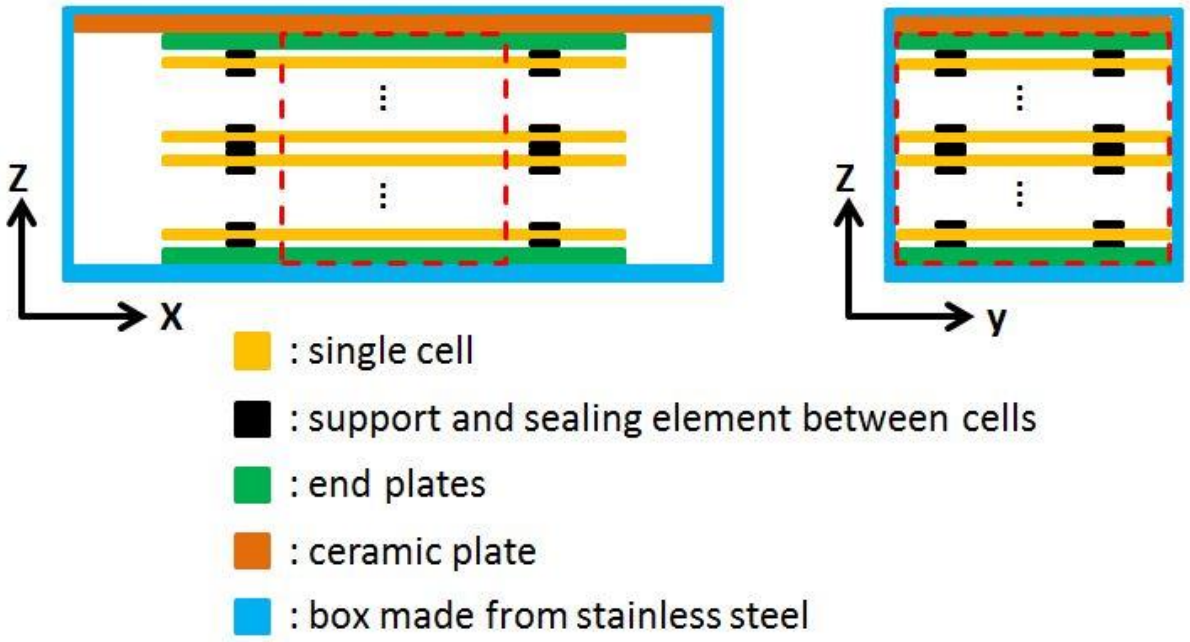

Figure 4.1: Schematic illustration of the stack used for this work

Internal reforming and co-electrolysis of H_2O and CO_2 are included within the scope of this model. Thus the following gas species are considered at the fuel side: H_2, H_2O, N_2, CO, CO_2 and CH_4, and O_2 and N_2 are considered at the air side. The three reactions shown in table 4.2 are modeled. Like many model developers assumed, carbon monoxide oxidation is neglected because conversion of CO through the water-gas shift is much faster (see chapter 3). Model is hierarchically built and is explained in the following sections.

Table 4.1: Some basic geometry parameters of the stack

Geometry parameter	Value	Unit
Length of reactive area	90	mm
Width of reactive area	142	mm
Thickness of air electrode	30	μm
Thickness of electrolyte	90	μm
Thickness of fuel electrode	30	μm

4.1 Model for the single repeat unit

The single repeat unit (SRU) is defined as the discretized element shown in figure 4.2, which is composed of the following parts: positive-electrolyte-negative structure (PEN), fuel channel, air channel and two interconnectors. It is worth noting, that the thickness of the SRU inter-connector is half of that of the whole interconnector. The fuel channel of the cell used for the work is filled with porous media (nickel foam). Model for the SRU lays the foundation for the whole modelling task.

As a hierarchical modelling method, model for the SRU is divide in different sub-models based on their functionalities. Besides sub-models of different SRU parts, two independent heat transfer sub-models are developed: one for the calculation of convective heat transfer between gas flow and channel wall, the other for calculating the conductive and radiative heat transfer between the PEN and the interconnector at air side. In this work, each component of the SRU is assumed to be a control volume with lumped parameters.

4.1.1 PEN model

Air electrode, electrolyte and fuel electrode are assembled in a triple layer often referred to as PEN. The main phenomena that occur in the PEN are: multicomponent gas diffusion through

porous electrodes, electrochemical reactions at TPB, transfer of oxygen ions through electrolyte as well as associated heat effect. Therefore, the PEN model primarily describes energy conservation, the reversible cell voltage and the different irreversible losses that arise from electrochemical reaction kinetic, charge transfer and mass transfer.

Table 4.2: Chemical reactions modeled and their ID number in the thesis

ID number	Equation
1	$H_2 + 0.5O_2 \rightleftarrows H_2O$
2	$CH_4 + H_2O \rightleftarrows 3H_2 + CO$
3	$CO + H_2O \rightleftarrows H_2 + CO_2$

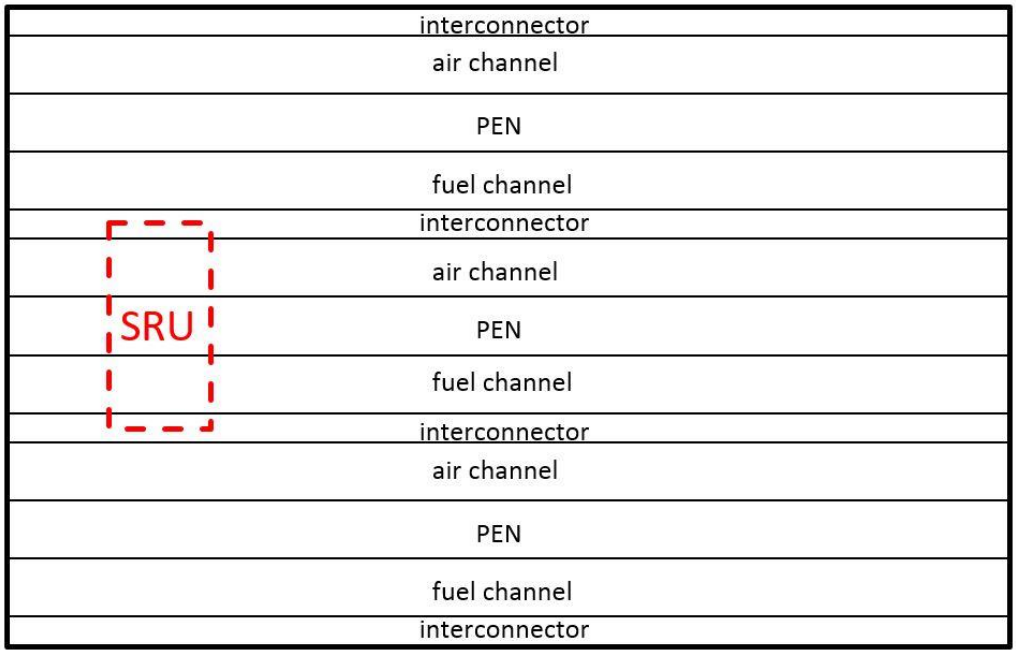

Figure 4.2: Definition of an SRU (in a schematic represented SOC stack)

The energy conservation equation is written considering that the heat of reaction for the electrochemical reactions is released (in fuel cell mode) or absorbed (in electrolysis cell mode) within the PEN and assuming that the heat production which corresponds to different voltage losses takes place in the PEN. This assumption is reasonable, because the heat generated due to ohmic resistances from interconnectors and contact resistances is negligible in comparison to the resistance offered by the electrolyte to diffusion of oxygen ions (Singhal and Kendall [2003]). The energy balance across the PEN is written as:

$$(\rho \cdot c \cdot \tau)_{PEN} \cdot l_{SRU} \cdot w \cdot \frac{dT_{PEN}}{dt} = \dot{Q}^{AC-PEN} + \dot{Q}^{FC-PEN} + \dot{Q}^{AI-PEN} + \dot{Q}^{PEN-PEN} - r_1 \cdot l_{SRU} \cdot w \cdot \Delta h_1 - j \cdot l_{SRU} \cdot w \cdot V, \tag{4.1}$$

where $\dot{Q}^{AC-PEN}$ and $\dot{Q}^{FC-PEN}$ are convective heat transfer rates between air and PEN and fuel and PEN, respectively, which are calculated in the convective heat transfer model; $\dot{Q}^{AI-PEN}$ is the conductive and radiative heat transfer rate between air side interconnector and PEN, which is calculated in the combined conductive and radiative heat transfer model; and $\dot{Q}^{PEN-PEN}$ is the sum of conductive heat transfer rates from and to adjacent units, which is calculated in the conductive heat transfer model. The three heat transfer models mentioned above are introduced later. In this thesis, a flux variable is considered positive when the flux flows into a component and vice-versa. In this model Δh_1 is the specific reaction enthalpy of hydrogen oxidation for both SOFC and SOEC mode. The reaction rate r_1 is related to the electric current density through the cell by Faraday's law

$$r_1 = \frac{j}{2F}. \tag{4.2}$$

The ideal reversible voltage is determined by the Gibb's free energy and according to the Nernst equation (see equation 2.11 and 2.12). For the electrochemical reactions considered here,

$$E = -\frac{\Delta g_1^0}{2F} - \frac{RT_{PEN}}{2F} \cdot \left(\ln \frac{x_{H_2O}}{x_{H_2} \cdot x_{O_2}^{0.5}} - \ln \frac{p^{0.5}}{p_0^{0.5}} \right). \tag{4.3}$$

p is the pressure of bulk flow which is mostly the same for both fuel and air flow. Δg_1^0 is the specific Gibb's free energy of hydrogen oxidation for both SOFC and SOEC mode under standard pressure and without considering the mixing effects, which can be derived from the standard Gibb's free energy of formation with the help of Gibbs-Helmholtz equation

$$\frac{\Delta g_1^0}{T_{PEN}} = \frac{\Delta g_1^0(T_0)}{T_0} + \Delta h_1^0 \cdot \left(\frac{1}{T_{PEN}} - \frac{1}{T_0} \right). \tag{4.4}$$

This equation is obtained based on an assumption that the reaction enthalpy Δh_1 is independent of temperature, which actually slightly changes over temperature. Around the operation temperature of this stack, this assumption results in an error of about $30mV$, which is subtracted from the calculated ideal voltage as a modification. As introduced in section 2.1, there are three kinds of irreversible losses: activation overpotential, ohmic overpotential and concentration overpotential. To represent the losses more precisely, activation overpotential is divided into fuel side and air side activation overpotential, same for the concentration overpotential. Thus this gives:

$$V = E - \eta_{act,an} - \eta_{act,ca} - \eta_{ohm} - \eta_{conc,an} - \eta_{conc,ca}. \tag{4.5}$$

Activation overpotential is described by Butler-Volmer equation (see equation 2.13). The B-V equation for fuel side and air side is written as:

$$j = j_{0,an} \cdot \left(exp\left(\frac{\alpha_{an} \cdot 2F\eta_{act,an}}{RT_{PEN}}\right) - exp\left(\frac{-(1-\alpha_{an}) \cdot 2F\eta_{act,an}}{RT_{PEN}}\right)\right), \tag{4.6}$$

$$j = j_{0,ca} \cdot \left(exp\left(\frac{\alpha_{ca} \cdot 2F\eta_{act,ca}}{RT_{PEN}}\right) - exp\left(\frac{-(1-\alpha_{ca}) \cdot 2F\eta_{act,ca}}{RT_{PEN}}\right)\right), \tag{4.7}$$

respectively. For the exchange current density j_0 at each electrode, the following semi-empirical equations are used (Wahl et al. [2015] and Njodzefon et al. [2013]):

$$j_{0,an} = \gamma_{an} T_{PEN} \cdot \left(\frac{p \cdot x_{H_2,TPB}}{p_0}\right)^a \cdot \left(\frac{p \cdot x_{H_2O,TPB}}{p_0}\right)^b \cdot exp\left(\frac{-E_{a,an}}{RT_{PEN}}\right), \tag{4.8}$$

$$j_{0,ca} = \gamma_{ca} T_{PEN} \cdot \left(\frac{p \cdot x_{O_2,TPB}}{p_0}\right)^d \cdot exp\left(\frac{-E_{a,ca}}{RT_{PEN}}\right). \tag{4.9}$$

It is assumed that the pressure gradient across the porous electrodes is negligible because the electrodes are extremely thin, especially for the electrolyte-supported cell used in this work. Therefore, gas pressure at TPB is considered equal to that of bulk flow p. Mole fraction of each component at TPB is calculated from equation 4.17-19.

Ohmic overpotential is the product of area specific resistance (ASR) and current density. The ASR in this model is divided into two parts (see equation 4.10): that of the PEN structure

whose basic parameters such as thickness and material are known and hence correlations for the conductivity of electrodes and electrolyte are usually available (see equation 4.11-13), and that of the rest components such as interconnectors and protective oxidative coatings which is also temperature dependent and derived by fitting a polynomial (see equation 4.14) to the electrochemical impedance spectroscopy (EIS) measurements.

$$ASR = \left(\frac{\tau_{an}}{\sigma_{an}} + \frac{\tau_{el}}{\sigma_{el}} + \frac{\tau_{ca}}{\sigma_{ca}}\right) + ASR_{rest} \tag{4.10}$$

$$\sigma_{an} = \frac{95 \times 10^6}{T_{PEN}} \cdot exp\left(\frac{-1150}{T_{PEN}}\right) \tag{4.11}$$

$$\sigma_{el} = \frac{5.15 \times 10^7}{T_{PEN}} \cdot exp\left(\frac{-10300}{T_{PEN}}\right) \tag{4.12}$$

$$\sigma_{ca} = \frac{42 \times 10^6}{T_{PEN}} \cdot exp\left(\frac{-1200}{T_{PEN}}\right) \tag{4.13}$$

The correlations for the above conductivities come from Hajimolana et al. [2011] and are valid for the YSZ electrolyte material.

$$ASR_{rest} = a_4 T_{PEN}^3 + a_3 T_{PEN}^2 + a_2 T_{PEN} + a_1 \tag{4.14}$$

Concentration overpotential here stems from the influence of the difference between gas components' concentrations in bulk flow and at TPB on the reversible voltage, which is derived from the Nernst equation as

$$\eta_{conc,an} = -\frac{RT_{PEN}}{2F} \cdot \left(\ln\frac{x_{H_2O}}{x_{H_2}} - \ln\frac{x_{H_2O,TPB}}{x_{H_2,TPB}}\right), \tag{4.15}$$

$$\eta_{conc,ca} = -\frac{RT_{PEN}}{4F} \cdot \left(\ln x_{O_2,TPB} - \ln x_{O_2}\right). \tag{4.16}$$

The concentration gradient exists because of mass transfer through the porous electrodes. For a multi component gas system considered in this work, the dusty gas model (DGM) is chosen to describe the species transfer process, as it is the most accurate among Fick's model, Stefan-Maxwell model and itself (Suwanwarangkul et al. [2003]). The three models mentioned are commonly used to model gas diffusion through porous media (He et al. [2014] and Veldsink et al. [1995]). The general form of DGM is implicit which usually results in longer computational time. However, explicit expressions for mole fractions at TPB of different gas compo-

nents can be analytically derived with the assumption of constant pressure throughout the porous electrode. The resultant equations are shown below (equation 4.17-19). Derivations are presented in appendix A.1.

For fuel side:

$$\begin{aligned} x_{H_2,TPB} = x_{H_2} &- \frac{RT_{PEN}\cdot j}{2F\cdot p}\cdot\left(\frac{1}{D^{eff}_{K,H_2}}+\frac{1}{D^{eff}_{H_2,H_2O}}\right)\cdot\tau_{an} \\ &- \sum_S\left\{\frac{\left(D^{eff}_{H_2,H_2O}-D^{eff}_{H_2,S}\right)\cdot D^{eff}_{H_2O,S}}{\left(D^{eff}_{H_2O,S}-D^{eff}_{H_2,S}\right)\cdot D^{eff}_{H_2,H_2O}}\cdot x_S\right. \\ &\left.\cdot\left[exp\left(\frac{RT_{PEN}\cdot j}{2F\cdot p}\cdot\left(\frac{1}{D^{eff}_{H_2,S}}-\frac{1}{D^{eff}_{H_2O,S}}\right)\cdot\tau_{an}\right)-1\right]\right\}, \end{aligned} \tag{4.17}$$

$$\begin{aligned} x_{H_2O,TPB} = x_{H_2O} &+ \frac{RT_{PEN}\cdot j}{2F\cdot p}\cdot\left(\frac{1}{D^{eff}_{K,H_2O}}+\frac{1}{D^{eff}_{H_2,H_2O}}\right)\cdot\tau_{an} \\ &+ \sum_S\left\{\frac{\left(D^{eff}_{H_2,H_2O}-D^{eff}_{H_2O,S}\right)\cdot D^{eff}_{H_2,S}}{\left(D^{eff}_{H_2O,S}-D^{eff}_{H_2,S}\right)\cdot D^{eff}_{H_2,H_2O}}\cdot x_S\right. \\ &\left.\cdot\left[exp\left(\frac{RT_{PEN}\cdot j}{2F\cdot p}\cdot\left(\frac{1}{D^{eff}_{H_2,S}}-\frac{1}{D^{eff}_{H_2O,S}}\right)\cdot\tau_{an}\right)-1\right]\right\}, \end{aligned} \tag{4.18}$$

where $S = \mathrm{N_2}, \mathrm{CO}, \mathrm{CO_2}\ and\ \mathrm{CH_4}$. For air side:

$$\begin{aligned} x_{O_2,TPB} = x_{O_2} &- \frac{RT_{PEN}\cdot j}{4F\cdot p}\cdot\frac{1}{D^{eff}_{K,O_2}}\cdot\tau_{ca} - x_{N_2} \\ &\cdot\left[exp\left(\frac{RT_{PEN}\cdot j}{4F\cdot p}\cdot\frac{1}{D^{eff}_{O_2,N_2}}\cdot\tau_{ca}\right)-1\right]. \end{aligned} \tag{4.19}$$

In the above three equations, the term $D^{eff}_{K,i}$ is the effective Knudsen diffusion coefficient of gas component i, and $D^{eff}_{i,j}$ is the effective binary diffusion coefficient of gas species i and j. Both effective diffusion coefficients are calculated by taking into account the effect of electrode porosity and tortuosity as:

$$D_{K,i}^{eff} = \frac{\varepsilon_{an/ca}}{tc_{an/ca}} \cdot D_{K,i}, \tag{4.20}$$

$$D_{i,j}^{eff} = \frac{\varepsilon_{an/ca}}{tc_{an/ca}} \cdot D_{i,j}. \tag{4.21}$$

$D_{K,i}$ is the Knudsen diffusion coefficient, which is defined by the kinetic theory of gases (Welty et al. [2009] and Chapman and Cowling [1970]) as

$$D_{K,i} = \frac{d_p}{3} \cdot \sqrt{\frac{8RT_{PEN}}{\pi M_i}}. \tag{4.22}$$

The binary diffusion coefficient $D_{i,j}$ at low to moderate pressures (such that the ideal gas behavior is valid) can be predicted with reasonable accuracy from the kinetic theory of gases using results from the Chapman-Enskog theory based on the Lennard-Jones potential (Bird et al. [2002]). This calculation theory is implemented into an online tool (Higgins and Binous [2013]), with which the binary diffusion coefficients of many binary systems at different temperatures and under various pressures can be easily gained. The coefficients at 310K and 1atm are first obtained from the tool and then corrected for other temperatures and pressures according to the Chapman-Enskog theory:

$$D_{i,j} = D_{i,j}(310K, 1atm) \cdot \left(\frac{T_{PEN}}{310}\right)^{1.75} \cdot \frac{p_0}{p}. \tag{4.23}$$

4.1.2 Fuel channel model

The relevant phenomena that are accounted for in the fuel channel are: mass storage, energy balance, pressure loss, methane reforming and its reverse reaction and water-shift and its reverse reaction. The model is developed under the following assumptions: ideal gas model applies to fuel gas; the channel behaves as a well-stirred reactor; nickel foam in the channel is always in thermal equilibrium with its surrounding gas; and there is no direct radiation between PEN and fuel side interconnector (see equation 4.1).

The mass of nickel foam is invariant, so only the gas phase is considered for the mass conservation:

$$l_{SRU} \cdot w \cdot \tau_{FC} \cdot \varepsilon_{FC} \cdot \frac{d\rho_{fuel}}{dt} = \dot{m}_{fuel,in} + \dot{m}_{fuel,out} + \frac{1}{2} r_1 \cdot l_{SRU} \cdot w \cdot M_{O_2}. \quad (4.24)$$

The component mass balance equations, one for each chemical species, can be written as

$$\begin{aligned} l_{SRU} \cdot w \cdot \tau_{FC} \cdot \varepsilon_{FC} \cdot & \frac{d(\rho_{fuel} \cdot y_i)}{dt} \\ & = \dot{m}_{fuel,in} \cdot y_{i,in} + \dot{m}_{fuel,out} \cdot y_i + M_i \\ & \cdot \left(l_{SRU} \cdot w \cdot \nu_{i,1} \cdot r_1 + l_{SRU} \cdot w \cdot \tau_{FC} \cdot \varepsilon_{FC} \cdot \sum_{j=2}^{3} \nu_{i,j} \cdot r_j \right), \end{aligned} \quad (4.25)$$

where $\nu_{i,j}$ is the stoichiometric coefficient of species i in the forward reaction j listed in table 4.2. It should be noted that i stands for 5 out of the 6 possible components of fuel gas, because the remaining component mass balance can be obtained from the equations for the 5 species and the mass conservation equation 4.24. The reaction rate r_1 is related to the current density (see equation 4.2). r_2 and r_3 is the net reaction rate of reaction 2 and 3 respectively (see table 4.2). Both are calculated using equations from Timmermann et al. [2010] in accordance with the Langmuir-Hinshelwood mechanism for heterogeneous catalytic reaction.

In the energy conservation equation the nickel foam is taken into account and results in the following equation:

$$\begin{aligned} l_{SRU} \cdot w \cdot \tau_{FC} \cdot \varepsilon_{FC} \cdot & \frac{d(\rho_{fuel} \cdot u_{fuel})}{dt} + l_{SRU} \cdot w \cdot \tau_{FC} \cdot (1 - \varepsilon_{FC}) \cdot \rho_{Ni} \cdot c_{Ni} \\ & \cdot \frac{dT_{fuel}}{dt} \\ & = \dot{m}_{fuel,in} \cdot h_{fuel,in} + \dot{m}_{fuel,out} \cdot h_{fuel} + \dot{Q}^{FC-PEN} \\ & + \dot{Q}^{FI-FC} + \dot{Q}^{FC-FC} - (-r_1 \cdot l_{SRU} \cdot w \cdot \Delta h_1), \end{aligned} \quad (4.26)$$

where the convective heat transfer rates $\dot{Q}^{FC-PEN}$ and $\dot{Q}^{FI-FC}$ are calculated in two convective heat transfer models and the heat conduction rate $\dot{Q}^{FC-FC}$ from and to adjacent control volumes owing to the nickel foam is calculated in a conductive heat transfer model. The enthalpy of reaction of hydrogen oxidation is subtracted in the above equation, because it is considered to be released or absorbed in PEN.

Momentum balance is not a key point in this work, because the pressure drop along the flow channel is very small due to the low flow velocity (Iwata et al. [2000]). Two choices of simplification for the momentum conservation equation are provided to the model user. The first is to replace the momentum equation with constant pressure. The second is a particular solution of the Navier-Stokes' equation for laminar flow of ideal gases with constant thermophysical properties between two infinite flat plates in steady-state:

$$\dot{m}_{fuel,in} = \rho_{fuel,in} \cdot \frac{w \cdot \tau_{FC}^3}{12\mu_{fuel}} \cdot \frac{p_{in} - p}{l_{SRU}}. \tag{4.27}$$

Though the convective heat transfer rate is calculated in a separate model, the heat transfer coefficient is determined in the flow channel model, because this is dependent upon the gas properties and channel structure. Two methods for determination are studied and compared with each other in section 5.2.2. The first is a constant convective heat transfer coefficient suggested by Aguiar et al. [2002] for the flow channel in SOC. The second is inspired by Yuan et al. [2001], where the authors develop a 3D CFD model based on the fully developed laminar flow assumption and with the boundary conditions that the PEN side has constant heat flux and the other sides are at constant temperature, and obtain good results. The same assumptions and boundary conditions are employed for this 1D model. In addition, for calculation of the heat transfer coefficient the hypothesis that the gas flows steadily between two infinite flat plates is introduced, which has also been adopted in many other non-CFD models (e.g. Aguiar et al. [2004], Larrain [2005] and Salogni and Colonna [2010]). Under these assumptions and boundary conditions and for the channel filled with porous material, a constant Nusselt number of $Nu = 12$ for PEN side and $Nu = 9.86$ for interconnector side are given in Bejan [2013]. Constant Nusselt number means that the heat transfer coefficient would change along the flow direction, because of the change in thermal conductivity of gas due to varying gas composition and temperature. It should be pointed out that heat conduction between PEN and nickel foam and between interconnector and nickel foam are included in the total conductive heat transfer. However, constant Nusselt number implies that the structure and porosity of the porous material do not influence the convective heat transfer and the derivation process is not provided in by the author. Therefore further study is suggested for a more precise simulation.

4.1.3 Air channel model

Phenomena occurring in the air channel are similar to and simpler than that in fuel channel. Primary differences between the two channels are that there is no nickel foam and no chemical reactions in the air channel. Besides, the width of air channel is smaller than that of fuel channel (see figure 4.3). While nickel foam functions as support and electric conductor in the fuel channel, the air side interconnector contacts with PEN to play a similar role. All the assumptions that are made for the fuel channel model, except those about nickel foam, hold true for the air channel model. Mass balance, component mass balance and energy balance are slightly different.

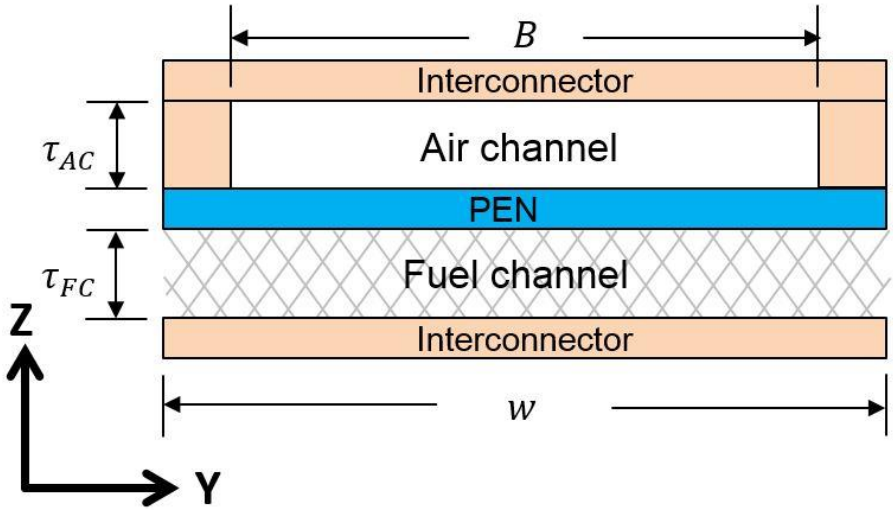

Figure 4.3: Illustration of different structures of fuel and air channel

Mass balance:

$$l_{SRU} \cdot B \cdot \tau_{AC} \cdot \frac{d\rho_{air}}{dt} = \dot{m}_{air,in} + \dot{m}_{air,out} - \frac{1}{2} r_1 \cdot l_{SRU} \cdot w \cdot M_{O_2}. \tag{4.28}$$

Component mass balance:

$$l_{SRU} \cdot B \cdot \tau_{AC} \cdot \frac{d(\rho_{air} \cdot y_i)}{dt} = \dot{m}_{air,in} \cdot y_{i,in} + \dot{m}_{air,out} \cdot y_i + M_i \cdot l_{SRU} \cdot w \cdot \nu_{i,1} \cdot r_1. \tag{4.29}$$

Energy balance:

$$l_{SRU} \cdot B \cdot \tau_{AC} \cdot \frac{d(\rho_{air} \cdot u_{air})}{dt} = \dot{m}_{air,in} \cdot h_{air,in} + \dot{m}_{air,out} \cdot h_{air} + \dot{Q}^{AC-PEN} + \dot{Q}^{AI-AC}. \quad (4.30)$$

Equation implemented to describe momentum balance in the air channel is the same as that for the fuel channel (see equation 4.27).

For the calculation of convective heat transfer coefficient between air flow and solid elements, two choices are studied and compared with each other like for the fuel channel. The first is the same as that described in the section above. The second is similar to that explained above. The same assumptions and boundary conditions are adopted, yet the values of Nusselt number are different. Since there is no porous media in the air channel, a constant Nusselt number of $Nu = 8.235$ for PEN side and $Nu = 7.54$ for interconnector side are obtained from Kakac et al. [2013].

4.1.4 Interconnector model

Heat storage is the only phenomenon modeled in this module. The interconnector function as an electric conductor is not considered, because electric current is assumed to flow directly out of and into PEN and the ohmic loss is lumped in the PEN model.

For fuel side interconnector:

$$(\rho \cdot c \cdot \tau)_{FI} \cdot l_{SRU} \cdot w \cdot \frac{dT_{FI}}{dt} = \dot{Q}^{FI-FC} + \dot{Q}^{FI-FI} + \dot{Q}^{FI-AI}, \quad (4.31)$$

where $\dot{Q}^{FI-FC}$ is already mentioned above, $\dot{Q}^{FI-FI}$ is the sum of heat conduction from and to the adjacent fuel side interconnector units along the x direction, and $\dot{Q}^{FI-AI}$ is the heat conduction to or from the air side interconnector of the adjacent cell.

For air side interconnector:

$$(\rho \cdot c \cdot \tau)_{AI} \cdot l_{SRU} \cdot w \cdot \frac{dT_{AI}}{dt} = \dot{Q}^{AI-AC} + \dot{Q}^{AI-PEN} + \dot{Q}^{AI-AI} + \dot{Q}^{AI-FI}, \quad (4.32)$$

where $\dot{Q}^{AI-AC}$ and $\dot{Q}^{AI-PEN}$ are introduced above, $\dot{Q}^{AI-AI}$ is the sum of heat conduction from and to the adjacent air side interconnector units along the x direction, and $\dot{Q}^{AI-FI}$ is the heat conduction to or from the fuel side interconnector of the adjacent cell.

4.1.5 Convective heat transfer model

This model calculates the heat convection rate with the temperature from the solid element module and the temperature and calculated heat transfer coefficient from the flow channel module:

$$\dot{Q} = \begin{cases} h \cdot l_{SRU} \cdot w \cdot (T_f - T_s), fuel\ side \\ h \cdot l_{SRU} \cdot B \cdot (T_f - T_s), air\ side \end{cases}. \tag{4.33}$$

4.1.6 Combined conductive and radiative heat transfer model

This model calculates the heat transfer rate between PEN and air side interconnector, since there exist both heat conduction and radiation effects between them (see figure 4.3):

$$\dot{Q} = \frac{\epsilon_{PEN} \cdot \epsilon_{AI}}{\epsilon_{PEN} + \epsilon_{AI} - \epsilon_{PEN} \cdot \epsilon_{AI}} \cdot \sigma \cdot (T_{PEN}^4 - T_{AI}^4) \cdot B \cdot l_{SRU} + \lambda \cdot \frac{T_{PEN} - T_{AI}}{\tau_{AC}} \cdot (w - B) \cdot l_{SRU}, \tag{4.34}$$

where the expression for heat radiation is that for the radiative heat transfer rate between two infinite flat plates which are grey bodies.

4.1.7 Connections of different modules

Model for the single repeat unit is built by connecting the different modules described in the preceding sections. Figure 4.4 illustrates the connections of different modules in an SRU. There are four kinds of flows that relate these modules: heat flow (heat convection between gas flow and solid elements, radiation between PEN and air side interconnector and heat conduction through interconnector), gas flow (in air and fuel channel), electric flow and information flow. The variables carried in the heat flow and the electric flow are so-called bilaterally coupled variables (Colonna and van Putten [2007]). One of the variables corresponds to a potential and the other to a flow. For example, voltage is the potential variable and electric current the flow variable. Variables carried by the gas flow are a pair of bilaterally coupled

variables plus specific enthalpy and gas composition. Information flow delivers variables needed for calculation purposes. For example, gas composition and pressure in flow channel module are required in PEN module to determine the multicomponent gas diffusion and associated effects; and electric current in PEN module is needed in both channel modules for calculating the reaction rate.

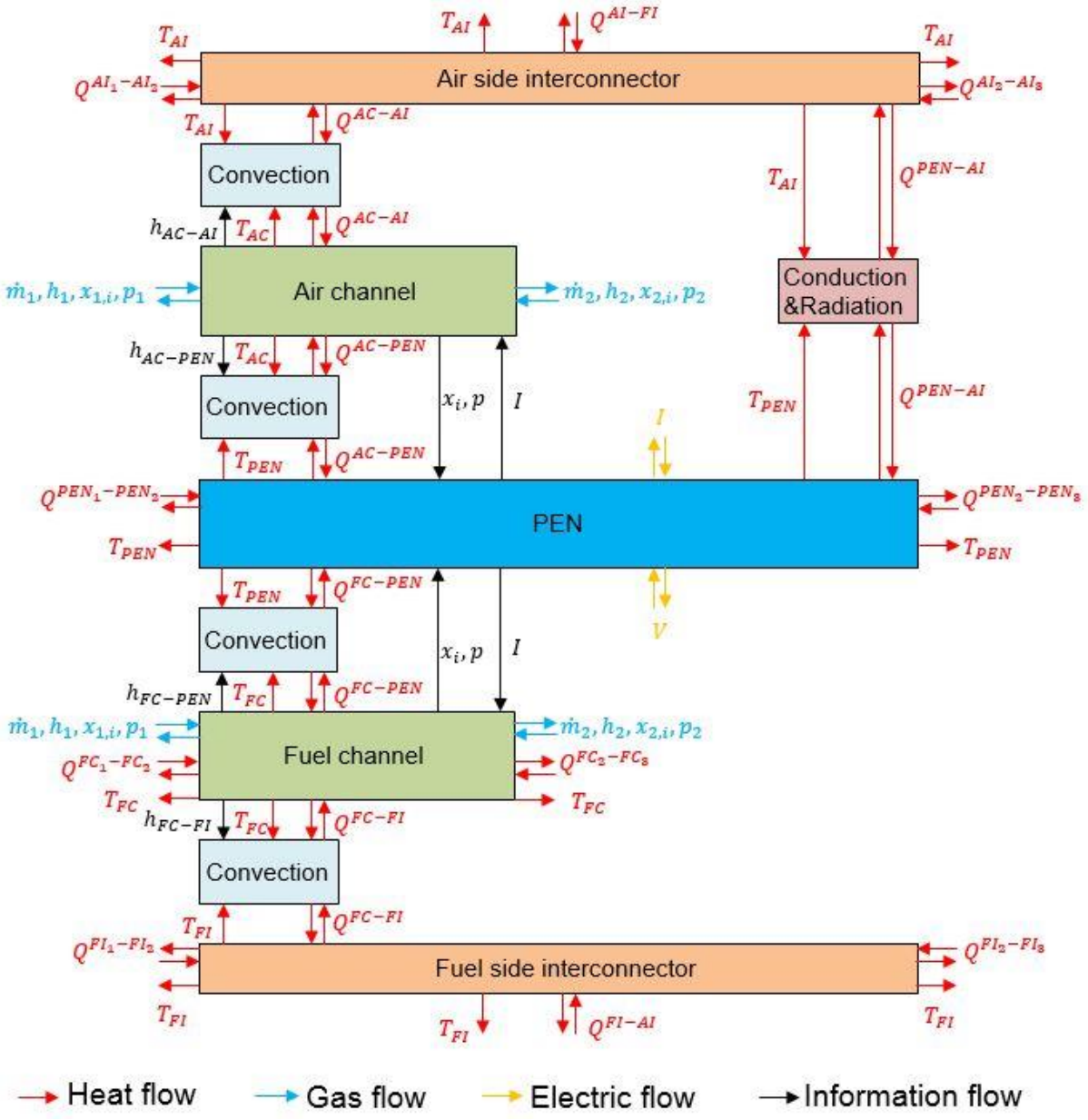

Figure 4.4: Causality diagram of an SRU model

4.2 Stack model

Stack model is developed on the basis of single repeat unit model. As is shown in figure 4.4, each single repeat unit interacts with its adjacent units or the surroundings of stack through three kinds of flows: heat flow, gas flow and electric flow.

4.2.1 Heat flow connections

Figure 4.5 shows the heat flow connections of a 3×3 stack model as an example. 3×3 means that the stack consists of 3 cells and each cell is discretized into 3 units in the model. These connections can be grouped into two kinds. The first is for the heat conduction between adjacent single repeat units. Similar to the convective heat transfer model, a model is built to calculate the heat conduction rate between two finite volumes with lumped parameters:

$$\dot{Q} = \lambda \cdot \frac{T_{\mathrm{I}} - T_{\mathrm{II}}}{l} \cdot A. \tag{4.35}$$

The second kind of connections is for the heat flow out of or into the stack. As this model is resolved in 1D+1D, only the heat flow along x and z direction can be directly implemented. The purpose of introducing the adaptor model (see figure 4.5) is to simplify the connection of stack module with other components, e. g. in a system-level modelling. One port needs only one connection, while several ports need several connections. The adaptor model consists of a vector of heat ports and a distributed heat port. Variables in a heat port are: a potential variable – temperature; and a flow variable – heat flow. Variables in a distributed heat port are a vector of temperatures and a vector of heat fluxes. Function of the adaptor model is to store temperatures and heat flows of all heat ports into the vector of temperatures and vector of heat fluxes of the distributed heat port, respectively.

As shown in figure 4.5, a simplification is employed: at the gas inlet side and gas outlet side, for each cell, the heat transfer along x direction and with its surroundings is “forced” to only flow through the PEN. This simplification is reasonable because a cell is very thin and hence the heat transfer inside a cell along z direction is much faster than that along x direction. This big difference between heat transfer rates along different directions can be confirmed by the fact that the temperature difference among different components in an SRU is much smaller than the temperature variation in a cell along x direction. There are three reasons for “forcing” all the heat to flow through PEN not one of the other components: 1. PEN is almost at the

middle of a cell; 2. PEN is the main heat source (during exothermic SOEC or SOFC mode) and heat sink (during endothermic SOEC mode); 3. PEN is the thinnest and its thermal conductivity is the smallest compared with other components, which means its ability to transfer heat along the x direction is the worst among all the components of an SRU, which results in a minimum effect of this simplification to the simulation result. In section 5.2.4 a comparison between the heat flow connections with and without the simplification is presented.

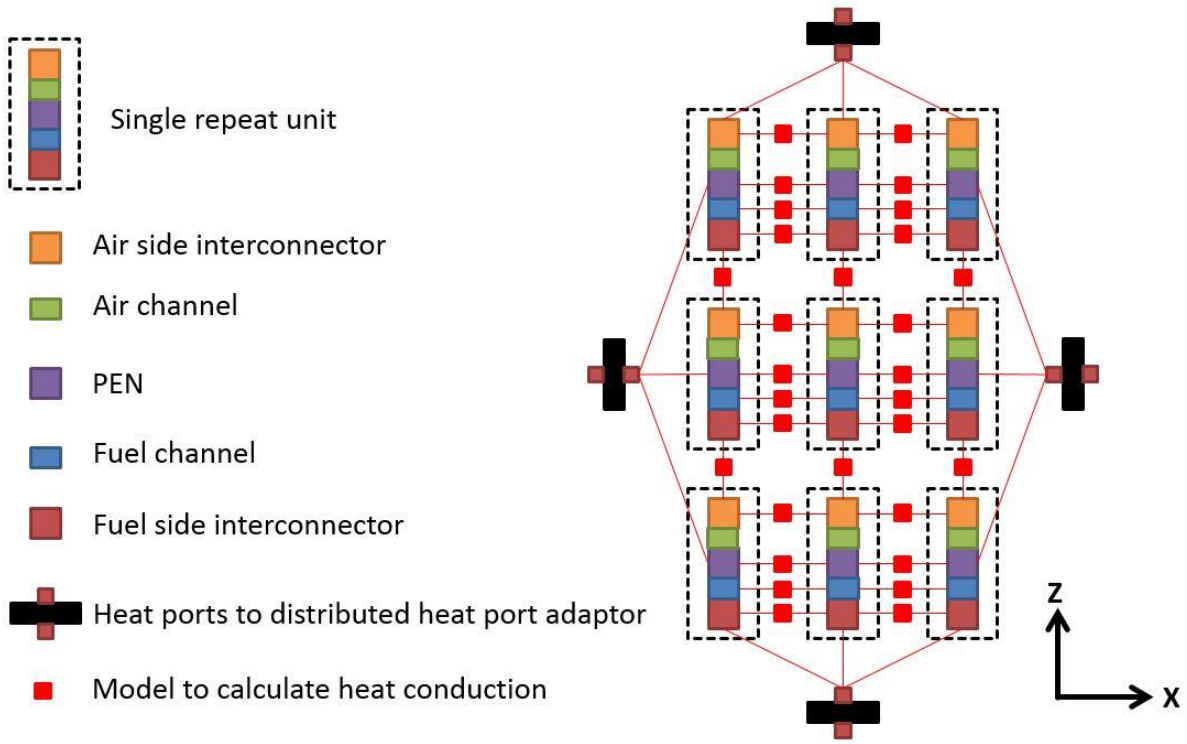

Figure 4.5: Schematic diagram of heat flow connections in a 3 × 3 stack model

4.2.2 Gas flow connections

Figure 4.6 illustrates gas flow connections of a 3 × 3 stack model as an example. The total inlet gas is distributed to each cell via a manifold. The gas exit of a discretization unit is connected with the gas inlet of the next discretization unit. For this work, it is assumed that the inlet gas is equally distributed among all cells. It is also possible to study the effects of non-uniform inlet gas distribution on the stack performance with this model by changing the hydraulic resistances of different pipelines of the manifold, which is the chosen parameter for determining gas distribution among different canals.

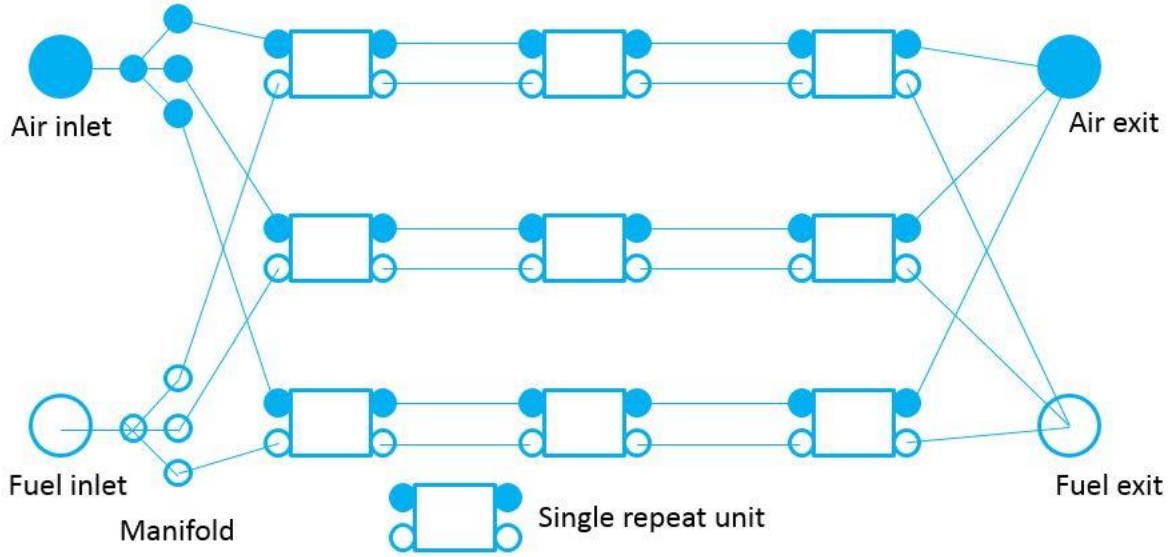

Figure 4.6: Schematic diagram of gas flow connections in a 3 × 3 stack model

4.2.3 Electric flow connections

Electric flow connections are simple compared to heat flow connections and gas flow connections. Single repeat units are connected in parallel to form a cell, and cells are connected in series to form a stack (see figure 4.7).

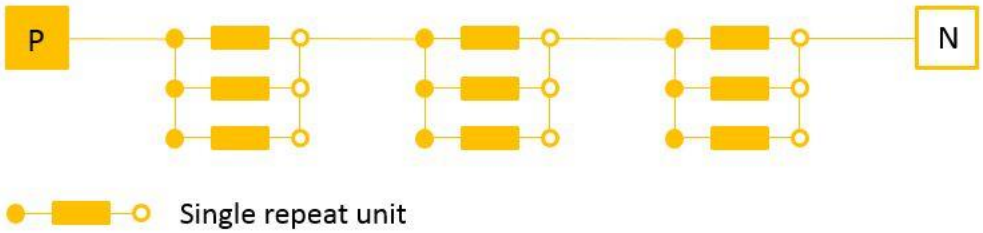

Figure 4.7: Schematic diagram of electric flow connections in a 3 × 3 stack model

4.2.4 Heat transfer between stack and its surroundings along y direction

As is explained in section 4.2.1, heat flow out of or into stack along y direction cannot be directly implemented (see figure 4.5). To provide the possibility to consider the heat transfer between stack and its surroundings along this direction, a Boolean named $sideHeatloss$ is introduced. If a user chooses $sideHeatloss = true$, a source term $\frac{T_{surroundings}-T_i}{R_i}$ is added to the right side of each of the energy conservation equations of SRU components (equation 4.1, 4.26, 4.30, 4.31 and 4.32), where i stands for PEN, fuel channel, air channel or interconnector and R_i is the total thermal resistance of the heat transfer along y direction between the SRU

component i and surroundings. This form of source term is chosen mainly to keep the flexibility and simplicity of the stack model. Each thermal resistance R_i is set as a parameter which should first be calculated by the user according to the actual circumstances and then provided as input to the model before simulation.

4.3 Modelling of heat transfer between stack and surroundings in the test bench

The modelling work should be validated with experiments. To accomplish the validation, heat transfer between the stack and the surroundings of the test bench where experiments are done should be modelled. This heat transfer condition has great influence especially on the temperature field inside the stack (see figure 5.9). As described in section 4.2.1 and 4.2.4, heat transfer between stack and surroundings along x and z direction is modelled outside of the stack model, while that along y direction is modelled as source terms in energy balance equations in the stack model where thermal resistance R_i should be determined.

4.3.1 Heat transfer along x and z direction

Since the actual circumstances determine the heat transfer, it is necessary to have an idea of the test bench structure. Figure 4.8 shows the simplified cross section of the test bench as well as heat transfer in the x- z plane. The temperature of the inner surface of the furnace is assumed to be well controlled and therefore uniform and constant during an experiment.

As is shown is the above figure, heat transfer paths between stack and surroundings along x and z direction are divided into three parts for modelling purposes. In this work, the "philosophy" of modelling heat transfer between stack and surroundings is to preserve the simplicity as along with a certain degree of accuracy, as this model is not a CFD model and should be suitable for integration into a system model. Thus, each of the red and yellow heat transfer paths in figure 4.8 is modelled as a series connection of a 1D conductive heat transfer resistance (see equation 4.36) and a heat capacity. It should be pointed out that the thermal resistance between stack and inner surface of box is neglected, because the heat carried by flowing gas travels very fast.

$$R = \frac{\tau}{A \cdot \lambda} \tag{4.36}$$

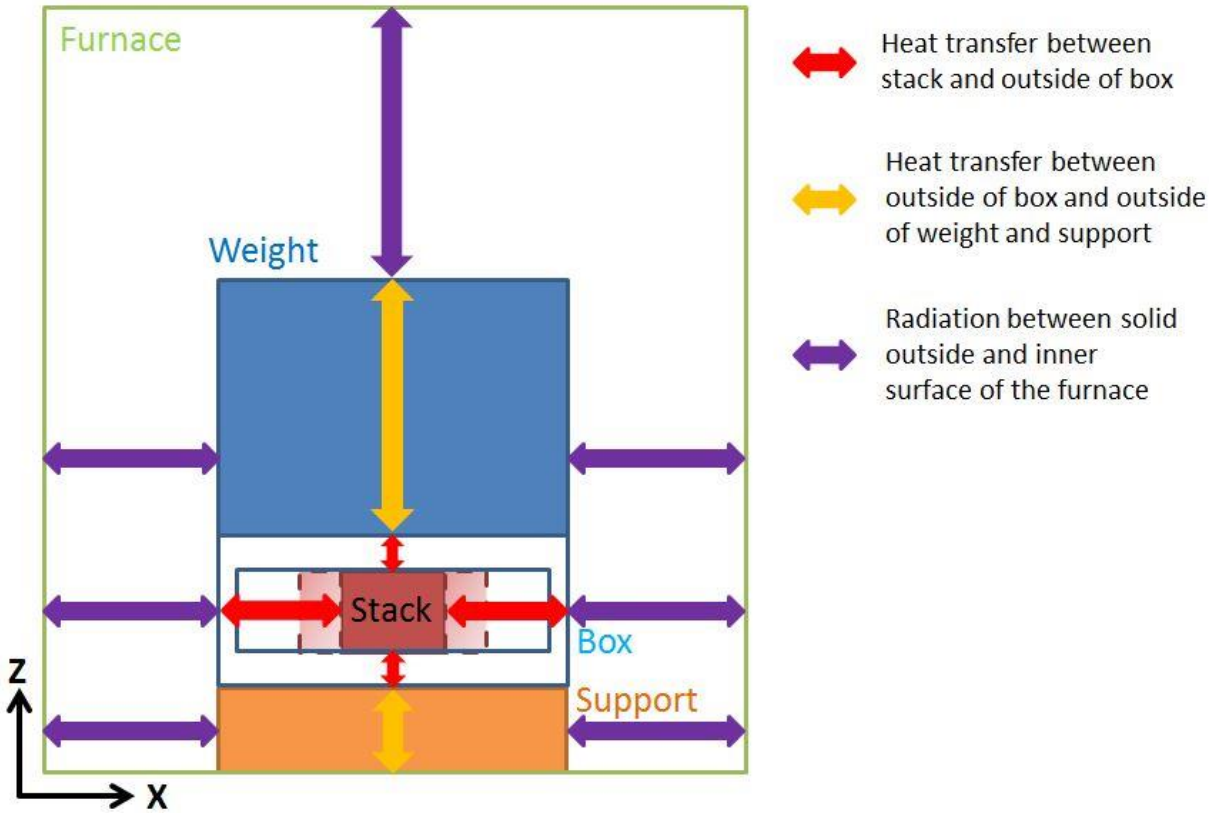

Figure 4.8: Schematic cross-sectional view of the test bench and heat transfer between stack and surroundings in x, z plane

Radiation is determined in a radiative heat transfer module, which calculates the radiation rate between two elements with lumped temperature with the following equation:

$$\dot{Q} = \epsilon_i \cdot \sigma \cdot \left(T_{furnace}^4 - T_i^4\right) \cdot A_i, \tag{4.37}$$

where i stands for the box, support or weight. This equation is obtained under the assumptions that all solids that participate are grey bodies, and the surface of furnace is much bigger so that view factor from surface of i to that of furnace is approximately equal to 1.

Figure 4.9 illustrates the structure of heat flow connections for modelling the heat transfer between stack and its surroundings along x and z direction in the test bench shown in figure 4.8. It is worth noting that the number of heat flow paths in the module for heat transfer from stack to outside of box should be equal to the size of the temperature vector and heat flux vector in the adaptor model which is connected to the module (see figure 4.5 and 4.9). Each of the paths in this module calculates the heat flow between a temperature node in the temperature vector of connected adaptor model and a lumped temperature node at the other side. It

should be noted that, to calculate the thermal resistance in the module for heat transfer from stack to outside of box along x direction, the cross-sectional area of a single cell should be used; to calculate the thermal resistance in the module for heat transfer from stack to outside of box along z direction, the cross-sectional area of a discretized unit should be used.

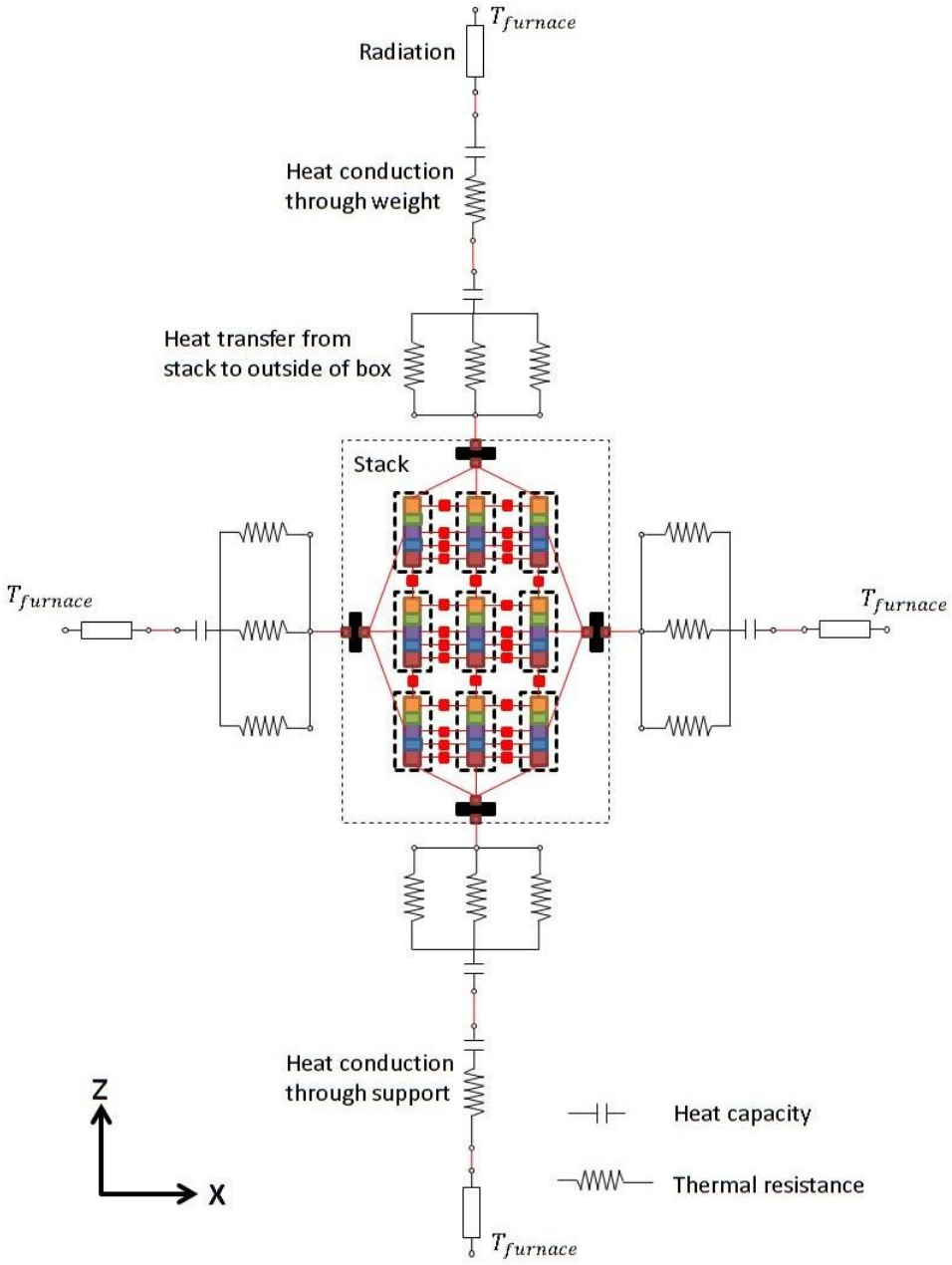

Figure 4.9: Heat flow connections of modeling of heat transfer between stack and surroundings along x and z direction in the test bench (an example with 3 × 3 stack)

4.3.2 Heat transfer along y direction

As is presented in section 4.2.4, the heat transfer between stack and surroundings along y direction is modeled with source terms in energy balance equations of SRU components, in

which the thermal resistance R_i should be determined in accordance with the practical situations.

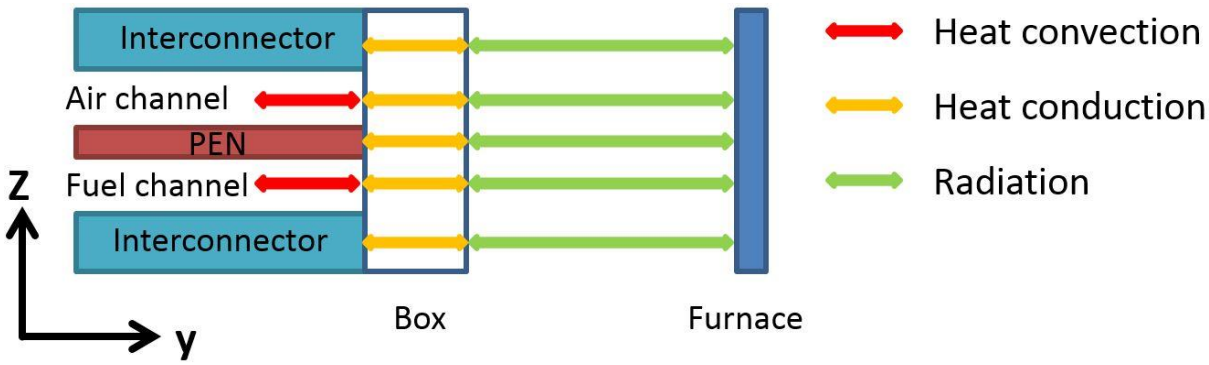

Figure 4.10: Illustration of heat transfer paths between components of an SRU and surroundings along y direction at one side in the test bench

Figure 4.10 shows how the thermal resistance R_i for each SRU component in this work is calculated. It should be pointed out that this figure only shows the heat flow along y direction at one side, while both sides should be considered by calculating R_i. For example, the thermal resistance between PEN and furnace along y direction at each side is composed of a series connection of a heat conduction resistance and a radiation resistance, and the total R_{PEN} is a parallel connection of the two series connections.

Thermal resistance of heat conduction is determined with the following equations:

$$R = \frac{1}{A \cdot h}, \tag{4.38}$$

$$h = \overline{Nu} \cdot \frac{\lambda}{l}, \tag{4.39}$$

$$\overline{Nu} = 0.664 \cdot Pr^{\frac{1}{3}} Re_l^{\frac{1}{2}}, \tag{4.40}$$

where l is the total length of flow channel and the expression for the average Nusselt number is that for external flow over a plate.

Thermal resistance of heat conduction can be calculated with equation 4.36, and that of radiation can be estimated with:

$$R = \frac{1}{4 \cdot \epsilon_{box} \cdot \sigma \cdot T_{furnace}^{3} \cdot A}, \tag{4.41}$$

which is the first order Taylor series expansion of the radiation term in equation 4.37.

4.4 Determination of parameters

4.4.1 Electrochemical parameters

Electrochemical parameters are very important, because they directly influence the relation between voltage and electric current of the stack which is one of the most crucial performance indicators. In this work, the electrochemical parameters are determined with different methods, which are described in the following. The experiments for determining these electrochemical parameters are performed within the research group at German Aerospace Center, therefore the methods are only briefly introduced in this work.

For the transfer coefficient α_{an} and α_{ca} in the B-V equations (see equation 4.6 and 4.7), the value 0.5 is applied, which is commonly used in many SOC models.

For all the parameters in equation 4.8 and 4.9 (γ_{an}, a, b, $E_{a,an}$, γ_{ca}, d and $E_{a,ca}$), values from Leonide et al. [2009] are adopted in the first phase of the work. In the second phase, these parameters are determined following the method described by Leonide et al. [2009], who develop the equivalent-circuit model by calculating and analyzing the corresponding distribution of relaxation times (DRT) of the impedance response, and then analyze the impedance spectra by a complex nonlinear least-squares (CNLS) approximation to a model function represented by the developed equivalent circuit. For more details about this method, readers can also refer to Schichlein et al. [2002] and Leonide et al. [2008]. Comparison is made in section 5.2.6 between simulations with values of these parameters from literature and those determined by means of impedance spectroscopy.

Determination of parameters a_1, a_2, a_3 and a_4 in equation 4.14 is a three-stage process. In the first step, the total ASR – temperature curve is obtained through impedance spectroscopy. Second, ASR of electrodes and electrolyte are calculated with correlations from literature (see equation 4.11-13) and subtracted from ASR obtained from impedance spectra to get ASR_{rest}. In the last step, the change of ASR_{rest} with temperature is fitted with a third order polynomial.

The structure parameters ε_{an}, ε_{ca}, tc_{an} and tc_{ca} of both electrodes directly affect the gas diffusion process and thus the concentration overpotential. The two porosities ε_{an} and ε_{ca} are given by the manufacturer of the stack used for this work. The tortuosity factors tc_{an} and tc_{ca} are determined by fitting to the experiment results.

4.4.2 Thermal properties

Thermal properties are important, as they significantly affect the temperature field inside the stack. Values of most of the thermal properties as input parameters into the stack model come from literature. These parameters are listed in table 4.3 together with their sources.

Table 4.3: Thermal properties from literature as input parameters in the stack model

Thermal property	Description	Source
c_{PEN}	Specific heat capacity of PEN	
ϵ_{PEN}	Emissivity of PEN surface	
λ_{PEN}	Thermal conductivity of PEN	Aguiar et al. [2004]
$c_{AI} = c_{FI}$	Specific heat capacity of interconnector	
$\epsilon_{AI} = \epsilon_{FI}$	Emissivity of interconnector surface	
$\lambda_{AI} = \lambda_{FI}$	Thermal conductivity of interconnector	

Effective thermal conductivity of the nickel foam in the fuel channel is difficult to be determined accurately because the effective thermal conductivity of porous media is affected by thermal conductivities of each phase, porosity and pore structure. Numerical methods are usually employed for precise prediction (Deng et al. [2017]). In this work, the following equation is adopted to reckon the effective thermal conductivity:

$$\lambda_{FC}^{eff} = \lambda_{Ni} \cdot \frac{\lambda_{fuel} + 2\lambda_{Ni} + 2\varepsilon_{FC} \cdot (\lambda_{fuel} - \lambda_{Ni})}{\lambda_{fuel} + 2\lambda_{Ni} - \varepsilon_{FC} \cdot (\lambda_{fuel} - \lambda_{Ni})}. \tag{4.42}$$

This equation is a deduced exact solution of the effective thermal conductivity in a homogenous continuous material with periodically distributed and non-interacting spherical pores (Eucken [1940]). Thermal conductivity of nickel foam in the stack is not yet measured and its pore structure is unknown, so the above chosen equation is an estimation.

Thermal properties of box, support and weight are needed for modeling of heat transfer between stack and furnace. Usually, these values can be found in the literature if the material of construction is known. Box and weight are made of a type of stainless steel and interconnector is also made of a kind of stainless steel. Thus, same values of specific heat capacity, thermal conductivity and emissivity of the interconnector are also used for box and weight. Support is made from a kind of refractory ceramics. A typical value of $1000 J/(kg \cdot K)$ for specific heat capacity of refractory ceramics is chosen from Schacht [2004]. A value of 0.4 is chosen for the emissivity of support, which is a typical value for ceramic fibre Al_2O_3 at the representative operating temperature of SOC (Benko [1991]). The typical value for thermal conductivity of refractory ceramics of $1 W/(m \cdot K)$ (Ewing et al. [1962]) is employed for thermal conductivity of the support. All values for the thermal properties of box, support and weight are approximate values, because the specific materials of these three components are unclear. However readers will find in the next chapter that simulations with these estimated values attain acceptable accuracy.

5 Results and discussion

This chapter is divided into three sections. In the first section, the selection of the axial discretization number for the single cell model is explained. In the second section, important characteristics of the model are highlighted. In the last section, the validation of the developed model with experiments is presented. The variables that are mainly concerned in this work are voltages and temperatures in the stack, because they are the most important variables for the stack operation. The voltage directly indicates the performance of a stack. Temperature field in the stack should be closely monitored and controlled during the operation because of the temperature limit of the materials, the strong interaction of voltage and temperature, and the decisive role of exit temperature to the waste heat utilization. Exactly speaking, the variables concerned are voltage of cell 5 and temperatures at points shown in figure 5.1, because they are measured in the experiments. T7, T8 and T9 is at the center of bottom cell (cell 1), middle cell (cell 5) and top cell (cell 10) of the stack respectively. T5 and T10 is at the 1/4 and 3/4 position along the length of cell 5, respectively.

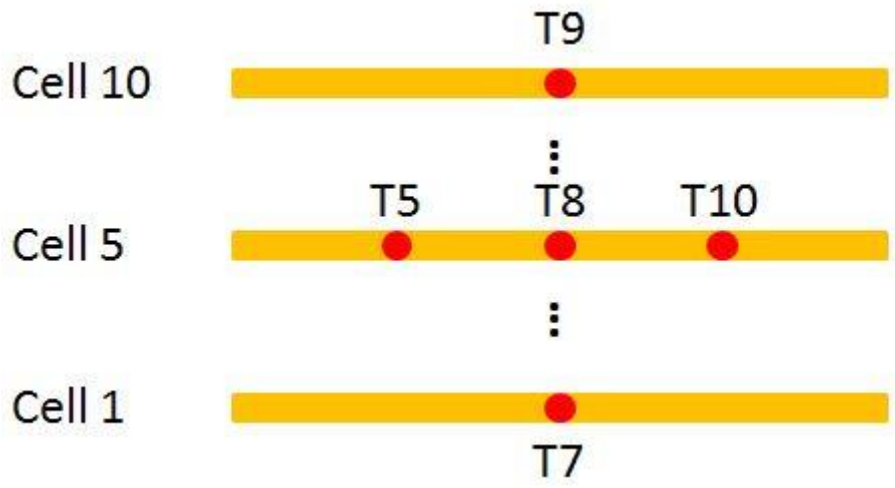

Figure 5.1: Temperature measuring points and ID number of cells

5.1 Determination of discretization number

Compromise between computational efficiency and accuracy is always an issue in the numerical simulation. The discretization number should be determined to reach a compromise between efficiency and accuracy according to the demand and computing power. Figure 5.2 shows the change of simulation results and computational time with discretization number. The temperature and voltage curves clearly exhibit an asymptotic behavior, while the compu-

tational time increases almost linearly. This observation should be kept in mind when choosing the discretization number. In this work, a discretization number of 10 is chosen.

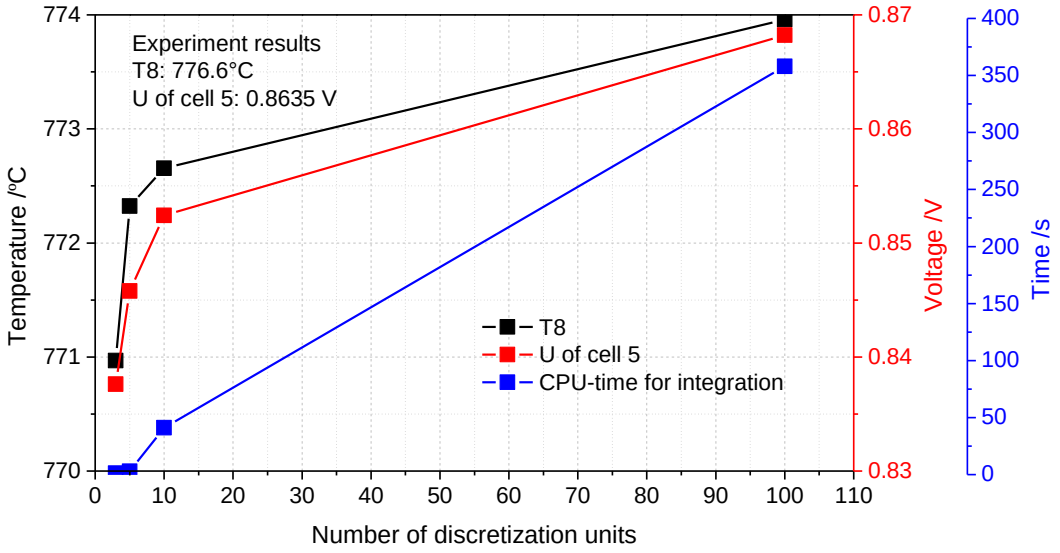

Figure 5.2: Influence of discretization number (SOFC; $p = 1.4bar$, $T_{furnace} = 750$°C, inlet $x_{H_2}:x_{N_2} = 40:60$, $FU = 0.55$, $j = 0.0798A/cm^2$; stop time: 1000000s)

5.2 Highlighting important characteristics of the model

5.2.1 Higher resolution of gas flow channels

To the author's knowledge, in the published non-CFD models for co- or counter-flow solid oxide cell or stack where the single cell is resolved along gas flow direction into discretization units, each gas flow channel is simply modeled as duct between two flat plates (e. g. in Sorrentino et al. [2008], Aguiar et al. [2004] and Salogni and Colonna [2010]). In this model the actual contact between PEN and air side interconnector as well as nickel foam that fills the fuel channel are included (compare figure 4.3 with figure 5.3) which leads to a higher resolution of both gas flow channels.

Figure 5.4 shows the difference between modelling without and with contact between PEN and air side interconnector. Temperature in the stack becomes lower, with considering the contact, for an exothermic SOEC mode where the PEN is a heat source because the heat transfer between PEN and air side interconnector is much faster. This means that the generated heat in the PEN can be transferred more quickly out of the stack, with the contact than that without. Explanation for the big change of heat flux can be found by looking into the law of heat conduction and law of heat radiation. Heat conduction rate is proportional to the tempera-

ture gradient, while heat radiation is proportional to difference of fourth power of temperature. For the heat transfer situation between PEN and air side interconnector, temperature difference between the two solid elements is small but the temperature gradient can be big due to the minimal space between them. Therefore heat conduction is much more dominant than heat radiation.

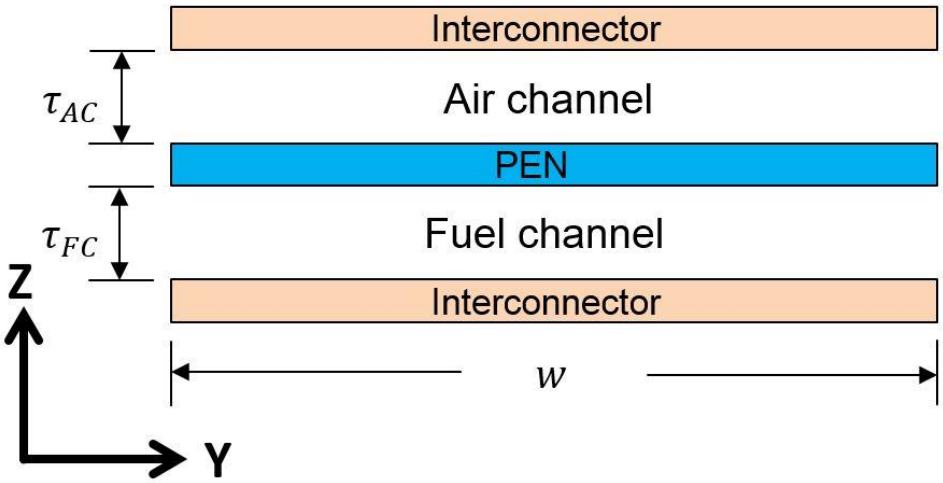

Figure 5.3: Illustration of gas flow channel structures considered in published non-CFD co-/counter-flow SOC models

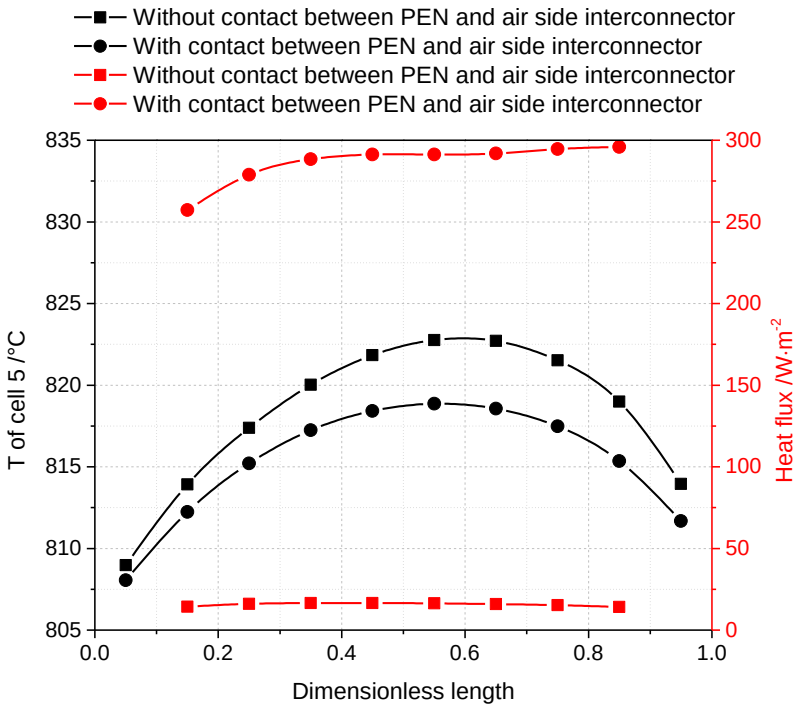

Figure 5.4: Effect of contact between PEN and air side interconnector on temperature of cell 5 and heat transfer between PEN and air side interconnector (SOEC; $p = 1.4bar$, $T_{furnace} = 800℃$, inlet $x_{H_2}: x_{H_2O} = 10:90$, $SU = 0.7$, $j = 0.5A/cm^2$)

Figure 5.5 illustrates the effect of nickel foam. Similar to the contact between PEN and air side interconnector, nickel foam also strengthens the heat transfer between stack and surroundings and causes the decrease of temperature inside the stack if the stack is exothermic. The nickel foam enhances heat transfer in two aspects: heat conduction through nickel foam along gas flow direction, and enhancement of convective heat transfer between fuel flow and solid elements. The improvement of heat convection by using porous inserts has been reported by many researchers and applied, e. g. in volumetric solar air receiver (Poulikakos and Kazmierczak [1987], Alkam et al. [2001] and Wu et al. [2011]).

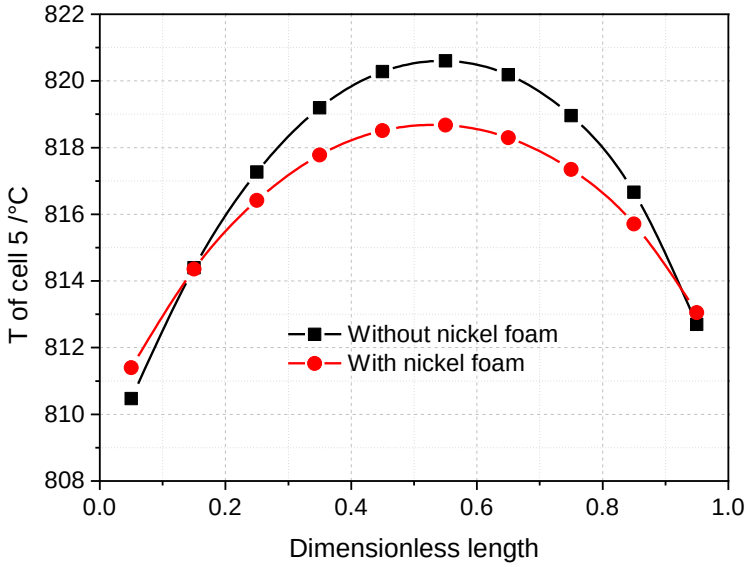

Figure 5.5: Effect of nickel foam in the fuel channel on the temperature distribution in stack (SOEC; $p = 1.4bar$, $T_{furnace} = 800℃$, inlet $x_{H_2}: x_{H_2O} = 10:90$, $SU = 0.7$, $j = 0.5A/cm^2$)

Discussion in this section shows the significance of higher resolution of gas flow channels in the model. Both the nickel foam and the contact between PEN and air side interconnector have notable influence on the temperature field in the stack.

5.2.2 Effect of heat convection model between gas flow and solid elements

In section 4.1.2, two methods for determining the convective heat transfer coefficient are mentioned. The first is to use constant heat transfer coefficient. The second is to use constant Nusselt number. Initially, purpose of comparing these two ways is to check which can predict the temperature inside the stack more accurately. The comparison results (see figure 5.6) indicate that the simulated heat convection is stronger with constant Nusselt number assumption than that using constant heat transfer coefficient, so that T8 corresponding to constant Nusselt

number is ca. 2.5℃ lower than that with constant heat transfer coefficient. Voltage of cell 5 predicted with constant Nusselt number assumption is a little bit higher, because lower temperature results in larger ohmic overpotential. However, the voltage difference is only ca. $6mV$ and actually negligible. An extra interesting finding is that the simulation is about 4 times faster using constant Nusselt number. The constant Nusselt number method is thus adopted, because the difference in predicting temperature is really small compared with the difference in computational time, and that computational efficiency is also very important especially for this model which should be applied in the next stage in system-level modelling. Reasons behind the great change in CPU-time are not further studied, because it is beyond the range of this master thesis work.

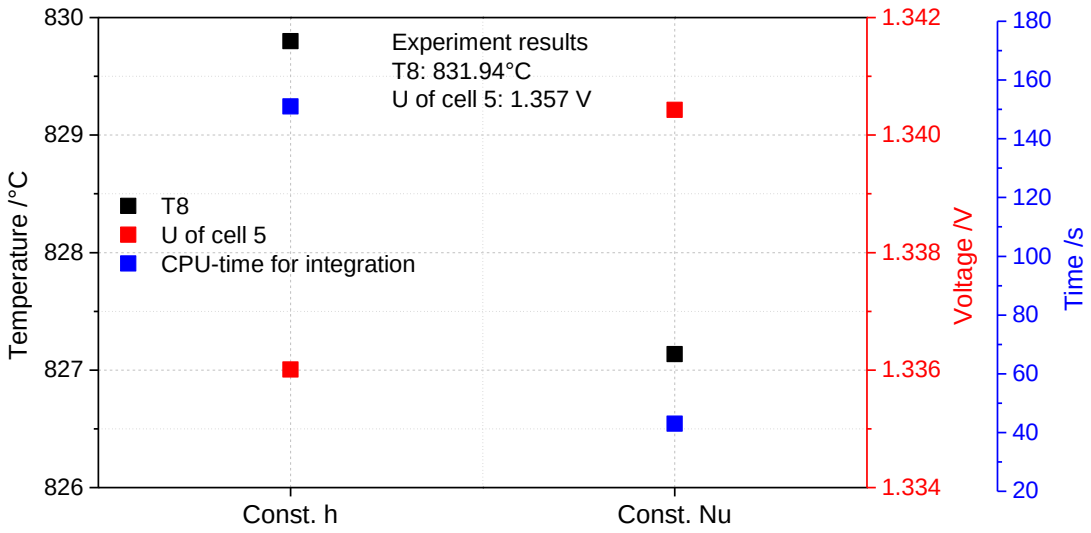

Figure 5.6: Comparison of two ways to model heat convection (SOEC; $p = 4bar$, $T_{furnace} =$ 800℃, inlet $x_{H_2}: x_{H_2O}: x_{N_2} = 7.92: 71.25: 20.83$, $SU = 0.7$, $j = 0.5025A/cm^2$; stop time: 1563827s)

5.2.3 Butler-Volmer equation and its inverse hyperbolic sine approximation

Butler-Volmer equation is an implicit expression of the activation overpotential, which may present an additional computational cost in numerical solution. Therefore, explicit inverse hyperbolic sine approximation of the B-V equation (compare equation 5.1 and 5.2 with equation 4.6 and 4.7) is also employed in the model as an attempt to increase computational efficiency.

Noren and Hoffman [2005] recommend this form of approximation because of its superior accuracy over the whole range of current density when $\alpha < 0.7$. However, results of simula-

tion with B-V equation and those with that approximation equation show remarkable difference between each other for the simulated operation condition corresponding to figure 5.7. Since the B-V equation describes the relation between current density and activation overpotential, its approximation directly influences the prediction of voltage. The predicted voltage of cell 5 with B-V equation is ca. $25mV$ lower, which means that the approximation of B-V equation brings about an overestimation of activation overpotential of ca. $25mV$ under the operation condition corresponding to figure 5.7. Higher overpotential means more electric energy is converted into heat (loss of electrical energy). Figure 5.7 shows that around $25mV$ overestimation of voltage loss leads to about 9℃ increase of T8 under the simulated operation condition. Though the deviation between experiment results and simulation results with B-V equation is even a little bigger than that with approximation equation in figure 5.7, it should be pointed out that the deviation with B-V equation mainly comes from inaccuracy of parameter values, while the simulation with approximation equation has at least two sources of errors, i.e. simplification of B-V equation and inaccuracy of parameter values.

$$\eta_{act,an} = \frac{RT_{PEN}}{\alpha_{an}F} \cdot \sinh^{-1}\left(\frac{j}{2j_{0,an}}\right) \tag{5.1}$$

$$\eta_{act,ca} = \frac{RT_{PEN}}{\alpha_{ca}F} \cdot \sinh^{-1}\left(\frac{j}{2j_{0,ca}}\right) \tag{5.2}$$

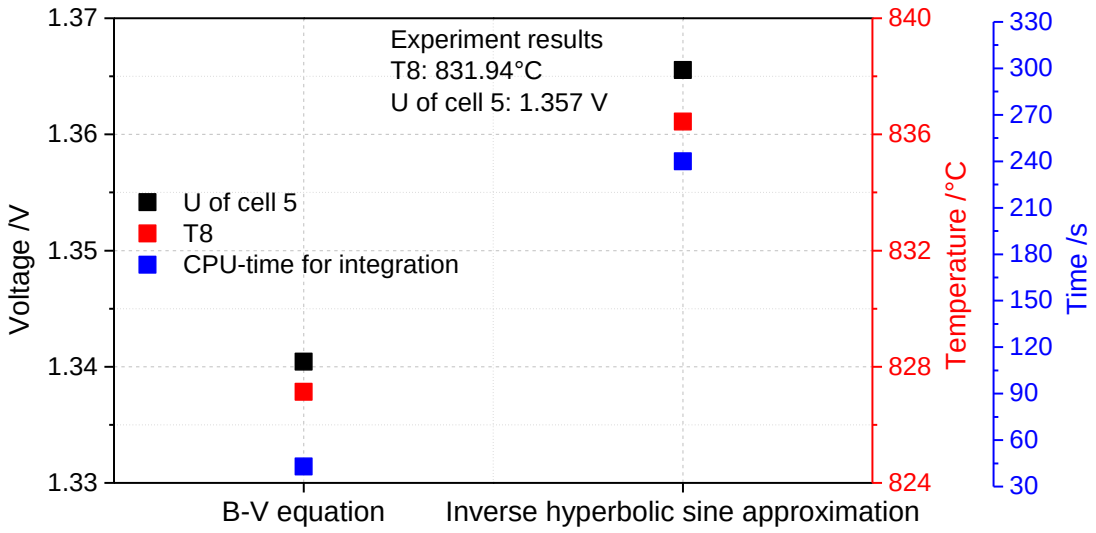

Figure 5.7: Comparison of B-V equation with its approximation (SOEC; $p = 4bar$, $T_{furnace} =$ 800℃, inlet $x_{H_2}: x_{H_2O}: x_{N_2} = 7.92: 71.25: 20.83$, $SU = 0.7$, $j = 0.5025A/cm^2$; stop time: 1563827s)

The change of CPU-time is unexpected. Simulation with B-V equation is almost 6 times quicker, which means that the use of approximation equation is meaningless. Explanation to

this phenomenon beyond expectation is not further explored for the same reason explained at the end of section 5.2.2.

5.2.4 Heat flow connections with and without simplification

In section 4.2.1 it is mentioned that a simplification for heat flow connections between stack and outside at the gas inlet side and gas exit side is employed. In this section the heat flow connections with and without this simplification are compared with each other. Figure 5.8 shows that the simplification almost does not influence simulation results (an explanation for this in section 4.2.1), but make the CPU-time drop dramatically. Thus, the simplified heat flow connections are adopted in this work.

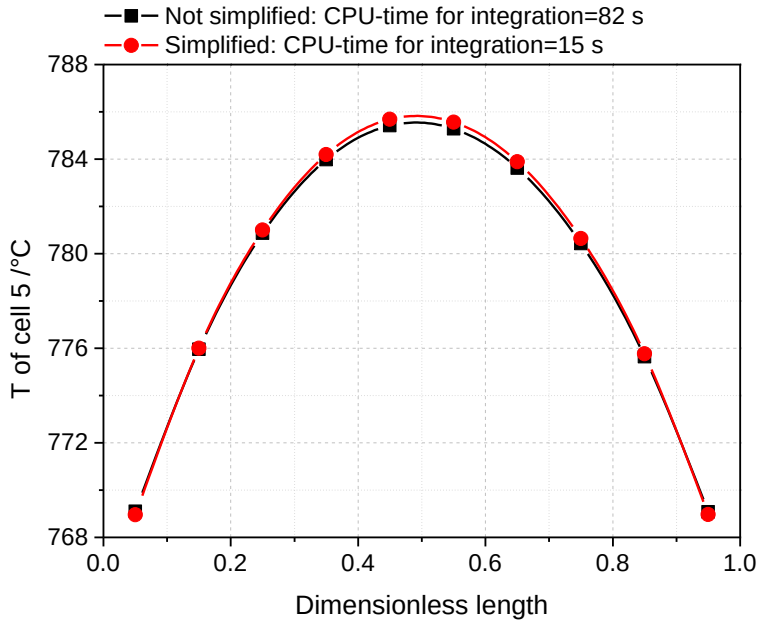

Figure 5.8: Comparison between simplified and not simplified heat flow connections (SOFC; $p = 1.4bar$, $T_{furnace} = 750$℃, inlet $x_{H_2}: x_{N_2} = 40:60$, $FU = 0.55$, $j = 0.0798A/cm^2$; stop time: 10000s; heat transfer between stack and surroundings along y not considered)

5.2.5 Importance of considering heat transfer between stack and surroundings

Figure 5.9 displays the great influence of heat transfer between stack and its surroundings upon the temperature field in the stack. Here the author wants to point out again that the stack modeled and mentioned in this work is actually the "effective volume" of a real stack (marked with red dash line in figure 4.1). Heat transfer between stack and surroundings along z direction significantly affects the value of maximum temperature and slightly flattens temperature distribution. Heat transfer between stack and surroundings along x direction remarkably influ-

ences not only the value of maximum temperature but also the position of hot spot. Heat transfer between stack and surroundings along y direction is relatively weak, because the stack used in this work consists of only 10 cells which means the height of stack is small and thus the surface area for heat transfer between stack and surroundings along y direction is relatively small. For stacks composed of more cells, heat transfer between stack and surroundings along y direction is expected to become more important. As conclusion, it is important to consider and carefully model the heat transfer between stack and its surroundings.

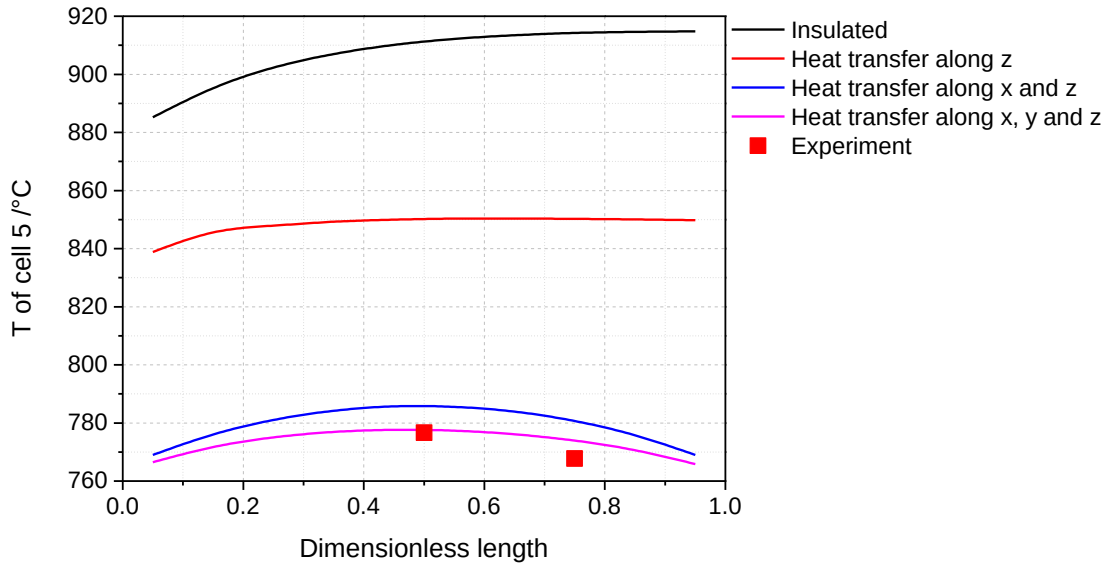

Figure 5.9: Effect of heat transfer between stack and surroundings (SOFC; $p = 1.4bar$, $T_{furnace} = 750$℃, inlet $x_{H_2}:x_{N_2} = 40:60$, $FU = 0.55$, $j = 0.0798A/cm^2$)

5.2.6 Electrochemical parameters determined by means of impedance spectroscopy

In section 4.4.1 it is introduced that for all the parameters in equation 4.8 and 4.9 values from literature are adopted in the first stage, and values obtained by analyzing data from electrochemical impedance spectroscopy (EIS) following methodology from the same literature are employed in the second stage. Simulations done in these two stages are compared with each other in figure 5.10. Compared with using parameters from literature, results given by the simulation with parameters that are more scientifically determined are closer to the experimental values. Under an SOEC mode, higher voltage as well as temperature are obtained with parameters determined by means of EIS. The higher voltage is due to higher activation overpotential, especially that of fuel electrode side (see figure 5.10(b)). This observation indicates that the cell used for this work has higher activation polarization loss than the cell identified

with the same method in that literature. This loss mainly origins from difference in fuel electrodes of these two kinds of cells. Temperature is also higher because more voltage loss means more heat production.

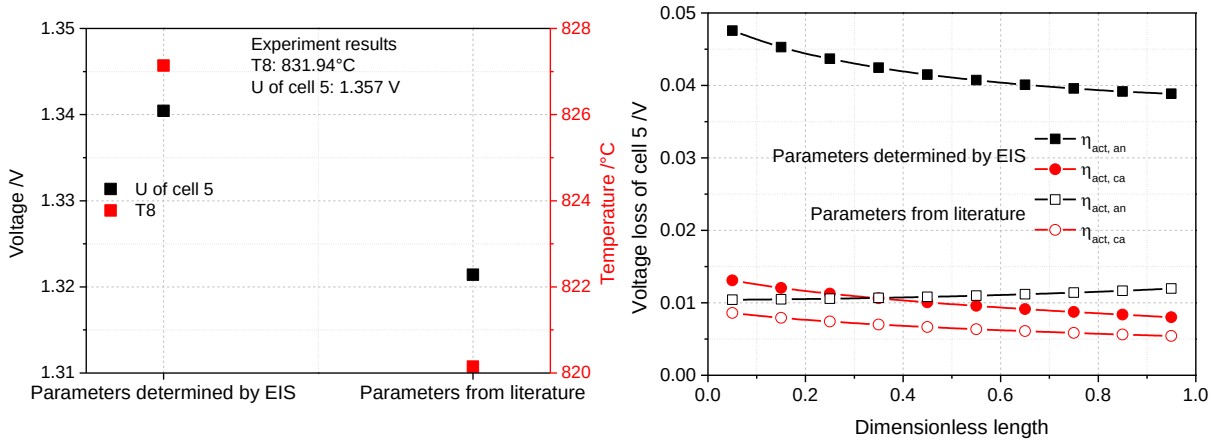

(a) (b)

Figure 5.10: Simulations with parameters determined by EIS and from literature (SOEC; $p = 4bar$, $T_{furnace} = 800℃$, inlet $x_{H_2}: x_{H_2O}: x_{N_2} = 7.92: 71.25: 20.83$, $SU = 0.7$, $j = 0.5025 A/cm^2$)

5.3 Validation with experiments

Since the stack model developed in this work only represent the "effective volume" (see figure 4.1), the temperature of the fluid within the manifold of the stack is not modeled, and the fuel and air temperatures at the inlet of "effective volume" are not measured, they have to be estimated. According to experimental measurements, temperature distribution of cell 5 usually shows a near-parabolic form (see figure 5.19), which means temperature changes along the length more quickly in entry and exit section than in middle section. Thus the gas inlet temperature of the "effective" stack is roughly estimated as:

$$\mathrm{T_{inlet}} = \mathrm{T5} - 2 \cdot (\mathrm{T8} - \mathrm{T5}) \tag{5.3}$$

It is assumed that both fuel and gas inlet possess the same temperature, and gas temperatures at entrance of each cell are equal.

5.3.1 Modification of Δh_1 from Modelica library

During the validation process, it is found that the value of Δh_1 obtained from the Modelica library is not accurate and about $3 KJ/mol$ smaller than the actual value around the operation

temperature of the stack used for this work (see figure 5.11). Therefore, the calculated Δh_1 is modified by adding $3KJ/mol$ to it in the model.

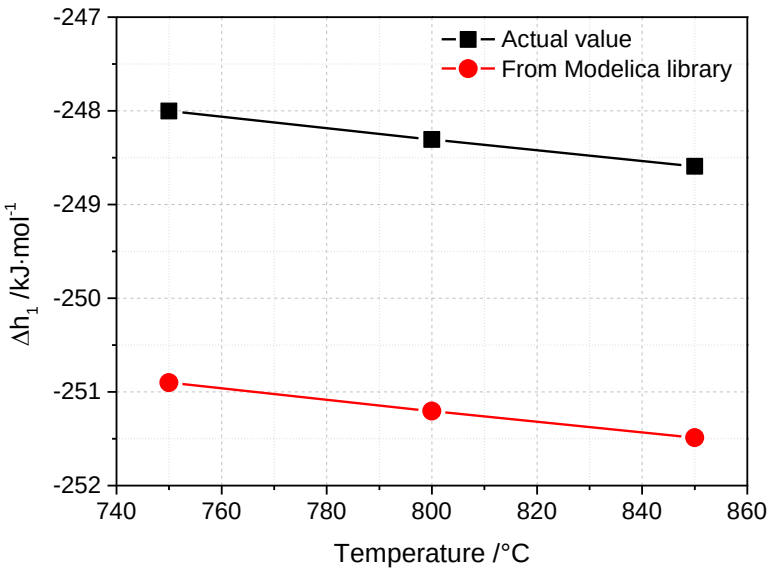

Figure 5.11: Deviation of Δh_1 calculated with Modelica library from the actual value

As the specific Gibb's free energy Δg_1^0 under standard pressure and without considering mixing effect, which participates in the calculation of ideal reversible voltage (see equation 4.3), is calculated in the model with Gibbs-Helmholtz equation and constant reaction enthalpy Δh_1^0 under standard condition (not Δh_1 calculated with Modelica library) (see equation 4.4), the deviation of Δh_1 from actual value mainly has influence on temperature in stack. The modification of Δh_1 causes temperature increase and slight voltage decrease for SOEC mode (see figure 5.12). This temperature change can be explained with the following equation:

$$\frac{\delta Q}{\Delta t} = j \cdot l_{SRU} \cdot w \cdot \left(\frac{\Delta h_1}{2F} + V\right), \tag{5.4}$$

where j is positive under SOFC mode and negative under SOEC mode, and δQ is negative for exothermic condition. This equation describes the heat production/consumption rate in a single repeat unit and is derived by substituting the Faraday's law (equation 4.2) into equation 5.5. Equation 5.4 can also explain why the influence of modification of Δh_1 upon the stack temperature is greater at higher current density. The slight change of voltage is resulted from the change of temperature: higher temperature mainly leads to lower ohmic resistance and thus lower voltage loss.

$$\frac{\delta Q}{\Delta t} = r_1 \cdot l_{SRU} \cdot w \cdot \Delta h_1 + j \cdot l_{SRU} \cdot w \cdot V \tag{5.5}$$

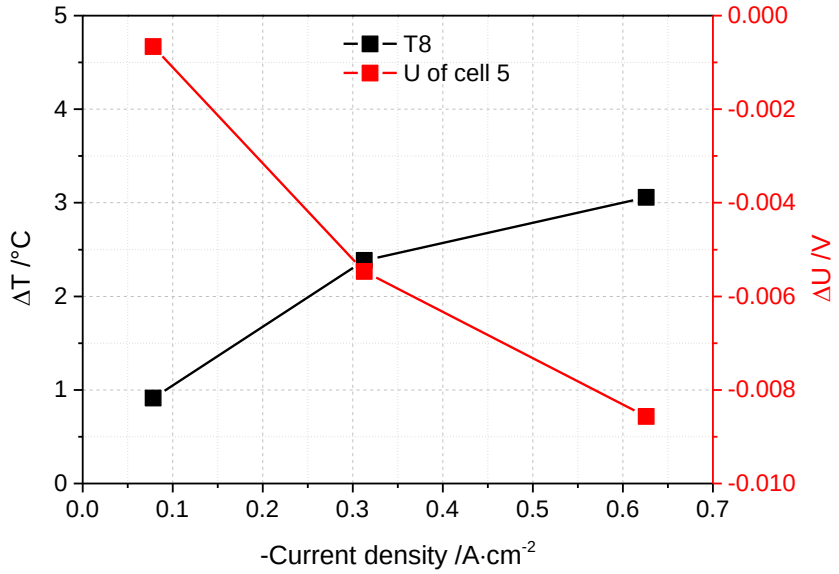

Figure 5.12: Change of temperature and voltage after modification of Δh_1 (SOEC; $p = 4bar$, $T_{furnace} = 800$℃, inlet $x_{H_2}: x_{H_2O} = 10:90$, $SU = 0.6$)

5.3.2 *V-j* and *T-j* curves

V-j and *T-j* curves are the most important and basic curves for characterizing cell or stack performance and are used here in validation.

5.3.2.1 Steady state process

Figure 5.13 and 5.14 show that, on the whole the model developed in this work can simulate steady state process for both SOFC and SOEC mode with reasonable accuracy. Average deviation of voltage of cell 5 is ca. $15mV$ for steady state SOFC points, and ca. $5mV$ for steady state SOEC points. However, it cannot be simply concluded from these results that this model can predict voltages under SOEC mode more accurately, because these results are only obtained from one set of steady state SOFC and SOEC experiments.

Maximum temperature deviation found for this set of steady state SOFC experiments and simulations is ca. 5℃ which appears when the temperature difference between stack and furnace reaches the highest value, while the maximum temperature deviation for the shown SOEC cases is ca. 7℃ and emerges when the stack is endothermic and the temperature difference between stack and surroundings peaks. These observations imply that: 1. the heat trans-

fer conditions between stack and surroundings may be different for exothermic stack and for endothermic stack; 2. increase of heat transfer rate between stack and surroundings with increasing temperature difference between them is probably underestimated in the model. The second hypothesis is reasonable because values of many thermal properties used in the model are taken from literature (see section 4.4.2), and some heat transfer paths are modeled with series connection of thermal resistance and heat capacity to keep simplicity.

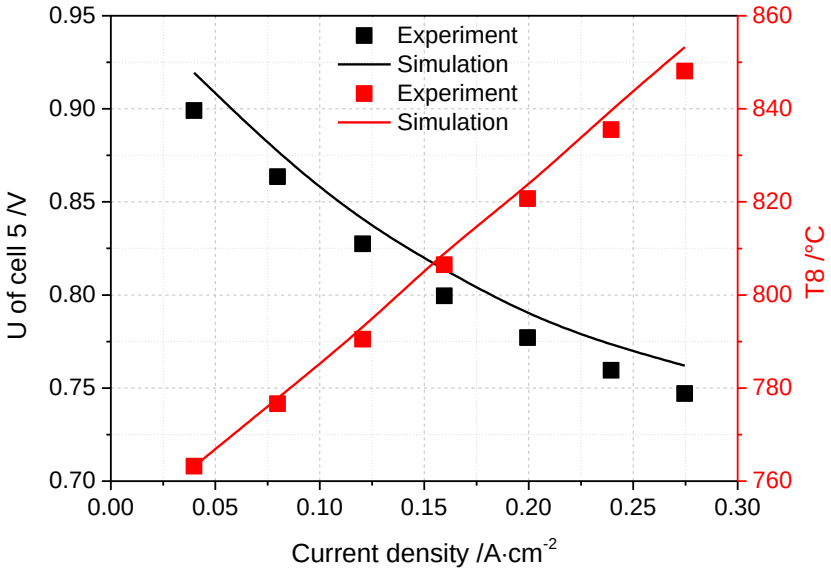

Figure 5.13: V-j and T-j curve (SOFC; $p = 1.4bar$, $T_{furnace} = 750$℃, inlet $x_{H_2}: x_{N_2} = 40: 60$, $FU = 0.55$)

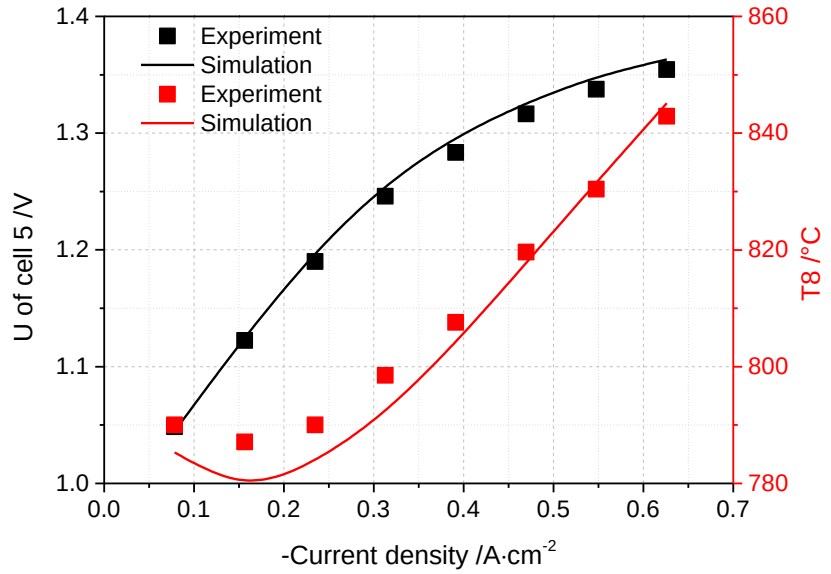

Figure 5.14: V-j and T-j curve (SOEC; $p = 4bar$, $T_{furnace} = 800$℃, inlet $x_{H_2}: x_{H_2O} = 10: 90$, $SU = 0.6$)

Figure 5.15 can partly prove the second hypothesis mentioned above. As an attempt, through raising the emissivity used to model radiation between box and furnace at gas inlet and exit side from 0.1 to 0.57, and raising the value of thermal resistance at each of these two sides by 100 times (see figure 4.8 and 4.9), resistance of radiation to the total heat transfer between stack and its surroundings is weakened and that of other heat transfer forms is enhanced. These changes make the heat transfer rate between stack and surroundings increase faster with increasing temperature difference between them, because radiation rate is proportional to difference of fourth power of temperature, while other two basic forms of heat transfer are only proportional to difference of first power of temperature. As expected, stack temperature gets closer to ambient temperature when temperature difference is large, and stays almost unchanged under low temperature difference condition.

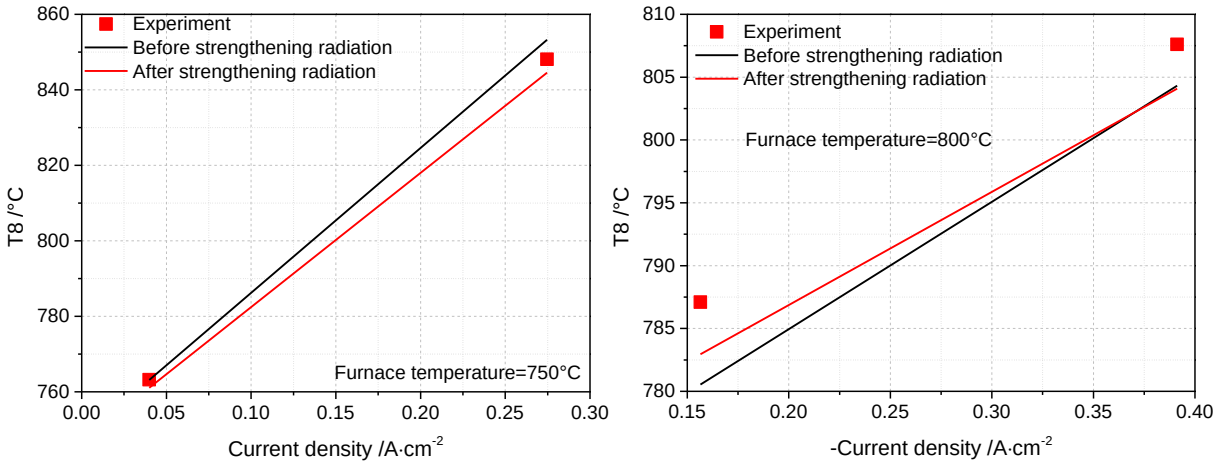

(a) SOFC; $p = 1.4bar$, inlet $x_{H_2}: x_{N_2} = 40: 60$, $FU = 0.55$

(b) SOEC; $p = 4bar$, inlet $x_{H_2}: x_{H_2O} = 10: 90$, $SU = 0.6$

Figure 5.15: Effect of strengthening radiation and weakening other heat transfer forms in the model

5.3.2.2 Dynamic process

Figure 5.16 and 5.17 show that, on the whole the model developed in this work can simulate dynamic process for both SOFC and SOEC mode with reasonable accuracy. Here the dynamic process means a ramp signal of current is given as an input.

The voltage deviation at low current density observed in figure 5.16 is anomaly, because voltage of cell 5 gained from simulation shows good consistence with experimental value for steady state SOFC, steady state SOEC and dynamic SOEC. Moreover, the experimental V-j

curve in figure 5.16 even displays a different form from the simulation curve at low current density region and this form is not typical for the V-j curve under SOFC mode (see figure 2.4). As all kinds of irreversible voltage losses are minimal at very low current density (see equations for different voltage losses in section 4.1.1), the voltage deviation must stem from the difference between the ideal reversible voltage calculated by the model and its actual value. An interesting finding from experiments with the same stack done by another researcher at German Aerospace Center is that, V-j curve shows similar form to that shown in figure 5.16 as long as "dry" fuel is employed, but displays typical form if there is steam in inlet fuel. The typical V-j curves shown in figure 2.4 are also obtained with experiments applying "wet" fuel. This interesting finding implies that the error in predicting the x_{H_2O} value in the beginning of a forward-scanning dynamic process using "dry" fuel is very likely to give rise to the voltage deviation. The mole fraction of steam is very small at low current density under these conditions (see figure 5.18(a)), and just a small error in x_{H_2O} can lead to a relatively big deviation in $\ln x_{H_2O}$ when x_{H_2O} is minimal due to the property of ln function (see figure 5.18(b)). According to equation 4.3, a deviation of ca. 2 in $\ln x_{H_2O}$ would induce a change of reversible voltage of ca. $0.1V$ around operation temperature of this stack.

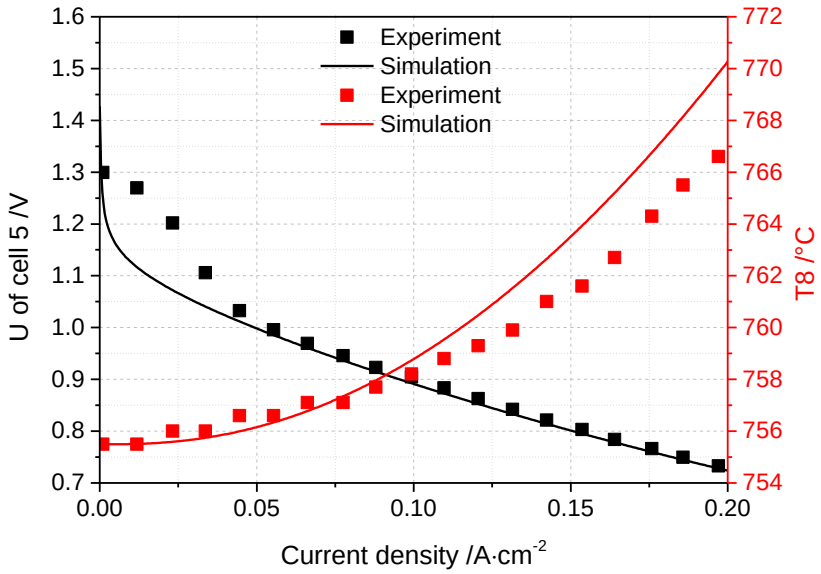

Figure 5.16: V-j and T-j curve (SOFC; $p = 1.4bar$, $T_{furnace} = 755.5$℃, inlet $x_{H_2}: x_{N_2} = 40:60$, $\Delta I/\Delta t = 10A/min$)

A hypothesis is put forward here to explain the probable error in predicting the steam mole fraction in the beginning of a forward-scanning dynamic process using "dry" fuel. In the beginning, steam production rate is very low because of the very small current density, and the

pores in the fuel electrode is barely filled with water molecules because "dry" fuel is applied. Therefore, most of the generated steam in the beginning phase leaves the triple phase boundary where it is produced, is adsorbed into the porous electrode and does not diffuse into the bulk fuel flow. This means that the actual x_{H_2O} in the start phase of the forward scan can be lower than that calculated in the model, because the porous electrodes are only considered as a "mass conductor" in the model and their "mass storage" effect is not implemented. This hypothesis can also explain the slope change of the experimental V-j curve in low current density region in figure 5.16. In the very beginning, the adsorption rate of steam is the highest and the influence of steam production on the ideal voltage is minimum, so the slope of V-j curve is almost zero. As the adsorption tends to saturation, the adsorption rate falls and the influence of steam production on the voltage ascends, so the absolute value of the slope increases. After the adsorption reaches saturation, effect of it upon the steam diffusion across porous electrode disappears, and V-j curve from experiment almost coincides with that obtained from simulation where the adsorption is not modeled.

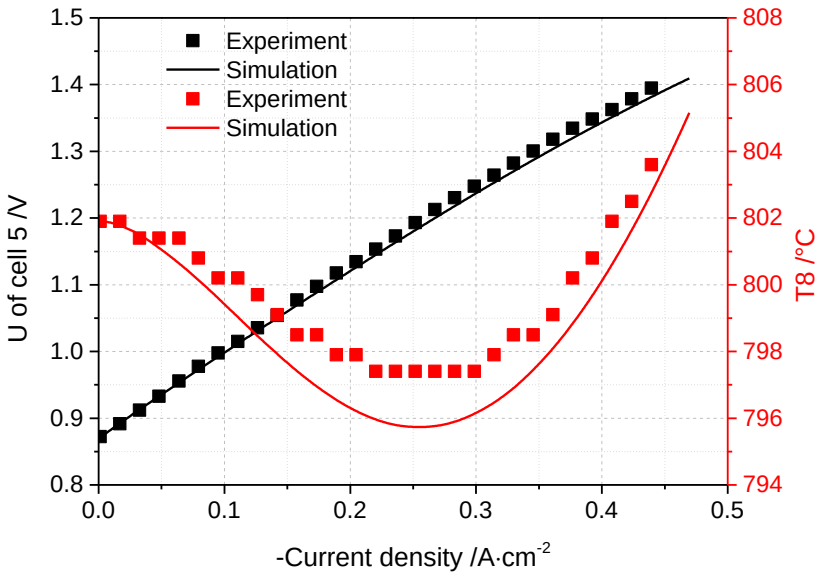

Figure 5.17: V-j and T-j curve (SOEC; $p = 4bar$, $T_{furnace} = 801.9℃$, inlet $x_{H_2}: x_{H_2O} = 10:90$, $\Delta I/\Delta t = 15A/min$)

Maximum temperature deviation is ca. 3℃ in figure 5.16 and ca. 2℃ in figure 5.17. It should be pointed out that the time duration of a dynamic process is very short (about 200 seconds) compared with the time needed to reach the steady temperature in a steady state process (at least 10000 seconds). Hence, the effect of heat transfer between stack and its surroundings is negligible in a fast dynamic process and the stack can be seen as insulated during this process. Therefore, the origins of the temperature deviation observed in dynamic process are different

from those observed in steady state process. Bigger temperature variation in the simulation of dynamic process than in the experiment implies that total thermal inertia or heat capacity of the stack is underestimated in the model. This is reasonable because values of many thermal properties used in the model are taken from literature (see section 4.4.2).

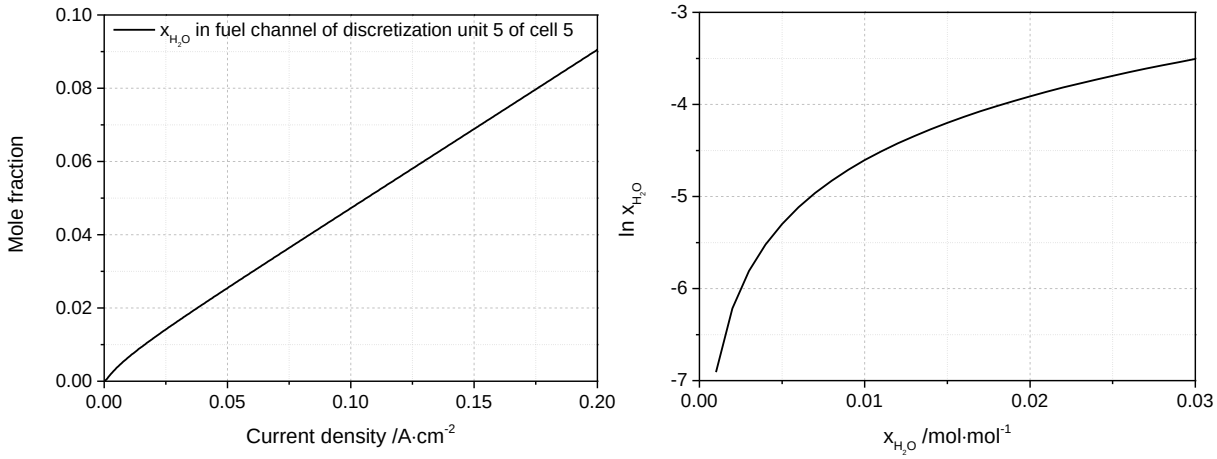

(a) Simulation result corresponding to figure 5.16 (b) ln x_{H_2O}-x_{H_2O} curve

Figure 5.18: Illustration of why small error of x_{H_2O} can cause relatively big error of ln x_{H_2O} at low current density

5.3.3 Spatial distribution of temperature field in the stack

Compared with 1D stack model the 1D+1D stack model developed in this work can provide more information on the temperature distribution in the stack. Figure 5.19 shows the ability of the 1D+1D stack model in predicting the temperature distribution along both x and z direction. On the whole, the form of temperature distribution along x and z direction can be represented in the model with reasonable accuracy. The temperature deviation is ca. 5℃ for cell 5 and ca. 7℃ for center of cell 10. For the case shown in figure 5.19, the hot spot in cell 5 is about at the middle in both experiment and simulation, temperature at 1/4 is higher than that at 3/4 of cell 5 in both experiment and simulation, and temperature at middle of cell 10 is lower than that at middle of cell 5 in both experiment and simulation. Temperature difference between center of cell 5 and center of cell 10 is larger in simulation, which indicates that the heat transfer between top of stack and outside may be overestimated and/or thermal resistance between cell 5 and cell 10 may be overestimated in the model.

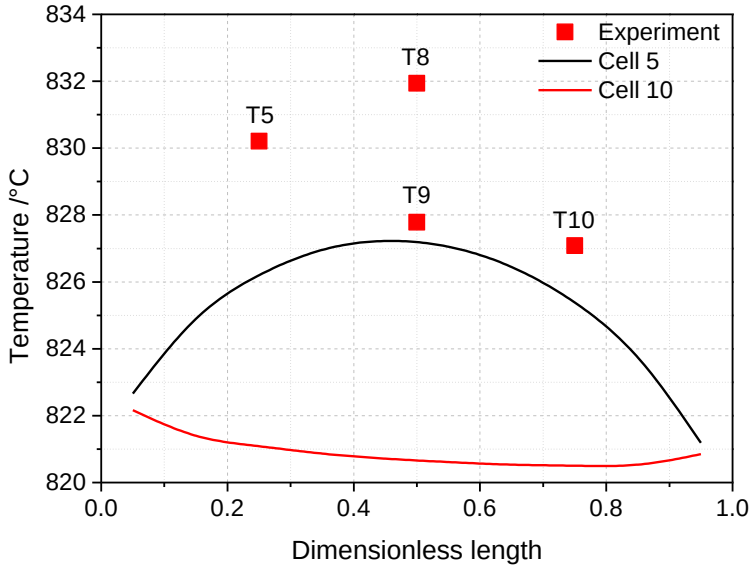

Figure 5.19: Temperature distribution in stack (SOEC; $p = 4bar$, $T_{furnace} = 800℃$, inlet $x_{H_2}: x_{H_2O}: x_{N_2} = 7.92: 71.25: 20.83$, $SU = 0.7$, $j = 0.5025 A/cm^2$)

6 Conclusion

6.1 Overview

Reversible solid oxide cell (rSOC) system is promising solution for energy storage. To study the steady state and dynamic characteristics of rSOC system and accelerate development of this technology, the Electrochemical Energy Technology group in the Institute of Engineering Thermodynamics of the German Aerospace Center aims at hierarchically developing an rSOC system model following a three-step strategy: 1. Develop model for single repeat unit which is a discretization unit of a single cell (see figure 4.2); 2. Develop model for a stack based on the single repeat unit model; 3. Develop model for system based on the stack model. This work is part of the three-step project and tasks of this work are refinement of the single repeat unit model and development of stack model.

The already existing single repeat unit model was refined in some aspects. The contact between PEN and air side interconnector as well as nickel foam in the fuel channel were implemented instead of just considering both gas channels as ducts between two flat plates. This higher resolution of both gas channels has proved to be meaningful, because both contact and nickel foam have great influence on the temperature distribution in the stack. The constant heat transfer coefficient assumption and constant Nusselt number assumption for heat convection between gas flow and solid elements were compared with each other, and the latter was chosen because computational efficiency is much higher with this assumption and the simulation results with both assumptions are quite close. Dusty gas model (DGM) for multicomponent gas diffusion in porous media was implemented to describe the gas diffusion process in porous electrodes instead of simple Fick's law in the previous version of the single repeat unit model. With the assumption that pressure gradient across the porous electrodes is zero, explicit expressions of mole fractions were analytically derived. For electrolyte-supported cell used in this work whose electrodes are very thin, diffusion process is very fast and thus difference between results with Fick's law and with DGM is minimal. For electrode-supported cell however, it is important to model the gas diffusion in electrodes precisely, because the electrode is relatively thick. With B-V equation the computational time is much shorter than that with its explicit inverse hyperbolic approximation, which is unexpected. For the parameters in the equations of exchange current densities (equation 4.8 and 4.9), values determined by means of impedance spectroscopy were employed instead of values from literature. Smaller deviation

between simulation and experiment results shows the necessity of determining these parameters through detailed experimental analysis.

Based on the refined single repeat unit model, a 1D+1D transient model of a co/counter-flow planar rSOC stack which is suitable for integrating into system modeling was developed. The stack model is adaptable to different thermal surroundings.

Before validating the stack model with experiments, the thermal surroundings of the stack in the test bench were modeled. To keep simplicity, the heat transfer between stack and furnace along x and z direction was modeled with series and/or parallel connections of thermal resistances, heat capacities and radiation modules (see figure 4.9). Since y direction is not considered in the 1D+1D model, heat transfer between stack and furnace along this direction was modeled as source terms in the energy balance equations of different components of single repeat unit (see section 4.2.4). Thermal resistance of each heat transfer source term is set as a parameter and should be estimated according to the boundary conditions of the problem, by the user, before simulation.

Validation was accomplished by comparing the change of voltage of cell 5 with current density, change of temperature at middle of cell 5 with current density, and temperatures at different positions. The stack model was successfully validated for both steady state and dynamic process and for both SOFC and SOEC mode.

6.2 Future work

Future work could be carried out in several directions:

- Since some material thermal properties are not given by the manufacturer of the stack used for this work, values from literature are adopted. This may be one of the reasons for the temperature deviations observed during the validation process (see figure 5.13-14, 5.16-17 and 5.19). Therefore, accurate values of these material thermal properties could be used and deviations could be possibly reduced.

- Degradation behavior is important for stack operation and could be included into the model.

- Stack model should be extended to stack module model with many stacks and insulation, as a first step towards a system model.

- The hypothesis put forward in section 5.3.2.2 to explain the voltage deviation observed in figure 5.16 could be verified by including the adsorption function of porous electrodes in the model and by using "wet" fuel for warming up and "dry" fuel for stack running in experiment.

- The transfer coefficient α_{an} and α_{ca} (in the B-V equation 4.6 and 4.7) could be determined through detailed experimental analysis and effects of values of the two coefficients could be analyzed.

References

Achenbach, E. "Three-dimensional and time-dependent simulation of a planar solid oxide fuel cell stack." *Journal of power sources* 49.1-3 (1994): 333-348.

Aguiar, Patricia, C. S. Adjiman, and Nigel P. Brandon. "Anode-supported intermediate temperature direct internal reforming solid oxide fuel cell. I: model-based steady-state performance." *Journal of power sources* 138.1 (2004): 120-136.

Aguiar, P., D. Chadwick, and L. Kershenbaum. "Modelling of an indirect internal reforming solid oxide fuel cell." *Chemical Engineering Science* 57.10 (2002): 1665-1677.

Alkam, M. K., M. A. Al-Nimr, and M. O. Hamdan. "Enhancing heat transfer in parallel-plate channels by using porous inserts." *International Journal of Heat and Mass Transfer* 44.5 (2001): 931-938.

Bae, Joong-Myeon, and B. C. H. Steele. "Properties of La 0.6 Sr 0.4 Co 0.2 Fe 0.8 O 3− δ (LSCF) double layer cathodes on gadolinium-doped cerium oxide (CGO) electrolytes: I. Role of SiO2." *Solid State Ionics* 106.3 (1998): 247-253.

Bejan, Adrian. *Convection heat transfer*. John wiley & sons, 2013.

Benko, I. "Energy conservation through increased emissivity in furnaces." *Periodica Polytechnica. Engineering. Mechanical Engineering* 35.4 (1991): 235.

Bird, R. Byron, Warren E. Stewart, and Edwin N. Lightfoot. *Transport phenomena, 2nd ed*. New York: John Wiley & Sons, 2002.

Casella, F., and P. Colonna. "Dynamic modeling of IGCC power plants." *Applied Thermal Engineering* 35 (2012): 91-111.

Casella, F., H. van Putten, and P. Colonna. "Dynamic simulation of a biomass-fired steam power plant: a comparison between causal and a-causal modular modeling." *Proceedings of the IMECE*. Vol. 7. 2007.

Chapman, Sydney, and Thomas George Cowling. *The mathematical theory of non-uniform gases: an account of the kinetic theory of viscosity, thermal conduction and diffusion in gases*. Cambridge university press, 1970.

Colonna, van Putten, and H. Van Putten. "Dynamic modeling of steam power cycles.: Part I—Modeling paradigm and validation." *Applied Thermal Engineering* 27.2-3 (2007): 467-480.

Deng, Zilong, et al. "Heat Conduction in Porous Media Characterized by Fractal Geometry." *Energies* 10.8 (2017): 1230.

Doherty, Wayne, Anthony Reynolds, and David Kennedy. "Process simulation of biomass gasification integrated with a solid oxide fuel cell stack." *Journal of Power Sources* 277 (2015): 292-303.

Doherty, Wayne, Anthony Reynolds, and David Kennedy. "Simulation of a tubular solid oxide fuel cell stack operating on biomass syngas using aspen plus." *Journal of the Electrochemical Society* 157.7 (2010): B975-B981.

Eucken, A. "Allgemeine gesetzmäßigkeiten für das wärmeleitvermögen verschiedener stoffarten und aggregatzustände." *Forschung auf dem Gebiet des Ingenieurwesens A* 11.1 (1940): 6-20.

Ewing, C. T., et al. "Thermal Conductivity of Refactory Materials." *Journal of Chemical and Engineering Data* 7.2 (1962): 251-256.

García-Camprubí, M., S. Izquierdo, and N. Fueyo. "Challenges in the electrochemical modelling of solid oxide fuel and electrolyser cells." *Renewable and Sustainable Energy Reviews* 33 (2014): 701-718.

Grondin, D., et al. "Computing approach of cathodic process within solid oxide electrolysis cell: Experiments and continuum model validation." *Journal of Power Sources* 196.22 (2011): 9561-9567.

Hajimolana, S. Ahmad, et al. "Mathematical modeling of solid oxide fuel cells: A review." *Renewable and Sustainable Energy Reviews* 15.4 (2011): 1893-1917.

He, Weidong, Weiqiang Lu, and James H. Dickerson. *Gas transport in solid oxide fuel cells*. New York: Springer, 2014.

Higgins, Brain G. and Housam Binous. "Binary diffusion coefficients for gases." Wolfram Demonstrations Project 2013. Available from: http://demonstrations.wolfram.com/BinaryDiffusionCoefficientsForGases/.

Iwata, Mitsunori, et al. "Performance analysis of planar-type unit SOFC considering current and temperature distributions." *Solid State Ionics* 132.3 (2000): 297-308.

Jin, Xinfang, and Xingjian Xue. "Mathematical modeling analysis of regenerative solid oxide fuel cells in switching mode conditions." *Journal of Power Sources* 195.19 (2010): 6652-6658.

Kakac, Sadik, Yaman Yener, and Anchasa Pramuanjaroenkij. *Convective heat transfer*. CRC press, 2013.

Karoliussen, H., K. Nisancioglu, and A. Solheim. "Use of effective conductivities and unit cell-based supraelements in the numerical simulation of solid oxide fuel cell stacks." *Journal of applied electrochemistry* 28.3 (1998): 283-288.

Klotz, D., et al. "Electrochemical model for SOFC and SOEC mode predicting performance and efficiency." *International Journal of Hydrogen Energy* 39.35 (2014): 20844-20849.

Laguna-Bercero, M. A., et al. "Steam electrolysis using a microtubular solid oxide fuel cell." *Journal of The Electrochemical Society* 157.6 (2010): B852-B855.

Larrain, Diego. "Solid oxide fuel cell stack simulation and optimization, including experimental validation and transient behavior." (2005).

Larrain, Diego, and Daniel Favrat. "Simulation of SOFC stack and repeat elements including interconnect degradation and anode reoxidation risk." *Journal of Power Sources* 161.1 (2006): 392-403.

Larrain, Diego, Daniel Favrat, and Michael Graetzel. *Modeling of cross-flow stack: sensitivity to thermal properties of the materials*. No. LENI-CONF-2003-007. 2003.

Laurencin, Jérôme, et al. "Modelling of solid oxide steam electrolyser: impact of the operating conditions on hydrogen production." *Journal of Power Sources* 196.4 (2011): 2080-2093.

Leonide, André, et al. "Evaluation and modeling of the cell resistance in anode-supported solid oxide fuel cells." *Journal of The Electrochemical Society* 155.1 (2008): B36-B41.

Leonide, Andre, Yannick Apel, and Ellen Ivers-Tiffee. "SOFC modeling and parameter identification by means of impedance spectroscopy." *ECS Transactions* 19.20 (2009): 81-109.

Mason, Edward Allen, and A. P. Malinauskas. *Gas transport in porous media: the dusty-gas model*. Vol. 17. Elsevier Science Ltd, 1983.

Menon, Vikram, et al. "A model-based understanding of solid-oxide electrolysis cells (SOECs) for syngas production by H 2 O/CO 2 co-electrolysis." *Journal of Power Sources* 274 (2015): 768-781.

Njodzefon, J-C., et al. "Electrochemical modeling of the current-voltage characteristics of an sofc in fuel cell and electrolyzer operation modes." *Journal of The Electrochemical Society* 160.4 (2013): F313-F323.

Noren, D. A., and M. A. Hoffman. "Clarifying the Butler–Volmer equation and related approximations for calculating activation losses in solid oxide fuel cell models." *Journal of Power Sources* 152 (2005): 175-181.

Riegraf, Matthias, et al. "Evaluation of the Effect of Sulfur on the Performance of Nickel/Gadolinium-Doped Ceria Based Solid Oxide Fuel Cell Anodes." *ChemSusChem* 10.3 (2017): 587-599.

Roos, M., et al. "Efficient simulation of fuel cell stacks with the volume averaging method." *Journal of Power Sources* 118.1 (2003): 86-95.

Salogni, A., and P. Colonna. "Modeling of solid oxide fuel cells for dynamic simulations of integrated systems." *Applied Thermal Engineering* 30.5 (2010): 464-477.

Schacht, Charles, ed. *Refractories handbook*. Vol. 178. CRC Press, 2004.

Schichlein, Helge, et al. "Deconvolution of electrochemical impedance spectra for the identification of electrode reaction mechanisms in solid oxide fuel cells." *Journal of Applied Electrochemistry* 32.8 (2002): 875-882.

Singhal, S. C. "Science and technology of solid-oxide fuel cells." *Mrs Bulletin* 25.3 (2000): 16-21.

Singhal, Subhash C., and Kevin Kendall, eds. *High-temperature solid oxide fuel cells: fundamentals, design and applications*. Elsevier, 2003.

Sorrentino, Marco, Cesare Pianese, and Yann G. Guezennec. "A hierarchical modeling approach to the simulation and control of planar solid oxide fuel cells." *Journal of Power Sources* 180.1 (2008): 380-392.

Spacil, Henry S. "Electrical device including nickel-containing stabilized zirconia electrode." U.S. Patent No. 3,503,809. 31 Mar. 1970.

Suwanwarangkul, R., et al. "Performance comparison of Fick's, dusty-gas and Stefan–Maxwell models to predict the concentration overpotential of a SOFC anode." *Journal of Power Sources* 122.1 (2003): 9-18.

Takahashi, Takehiko, ed. *High conductivity solid ionic conductors: recent trends and applications*. World Scientific, 1989.

Timmermann, H., et al. "Kinetics of (reversible) internal reforming of methane in solid oxide fuel cells under stationary and APU conditions." *Journal of Power Sources* 195.1 (2010): 214-222.

Uchida, Hiroyuki, Hiroaki Suzuki, and Masahiro Watanabe. "High-Performance Electrode for Medium-Temperature Solid Oxide Fuel Cells Effects of Composition and Microstructures on Performance of Ceria-Based Anodes." *Journal of the Electrochemical Society* 145.2 (1998): 615-620.

Poulikakos, Dimos, and M. Kazmierczak. "Forced convection in a duct partially filled with a porous material." *Journal of Heat Transfer* 109.3 (1987): 653-662.

Veldsink, J. W., et al. "The use of the dusty-gas model for the description of mass transport with chemical reaction in porous media." *The Chemical Engineering Journal and the Biochemical Engineering Journal* 57.2 (1995): 115-125.

Wahl, Stefanie, et al. "Modeling of a thermally integrated 10 kW e planar solid oxide fuel cell system with anode offgas recycling and internal reforming by discretization in flow direction." *Journal of Power Sources* 279 (2015): 656-666.

Welty, James R., et al. *Fundamentals of momentum, heat, and mass transfer*. John Wiley & Sons, 2009.

Wu, Zhiyong, et al. "Numerical simulation of convective heat transfer between air flow and ceramic foams to optimise volumetric solar air receiver performances." *International Journal of Heat and Mass Transfer* 54.7-8 (2011): 1527-1537.

Xie, Yuanyuan, and Xingjian Xue. "Modeling of solid oxide electrolysis cell for syngas generation with detailed surface chemistry." *Solid state ionics* 224 (2012): 64-73.

Yamamoto, Osamu, et al. "Electrical conductivity of stabilized zirconia with ytterbia and scandia." *Solid State Ionics* 79 (1995): 137-142.

Yuan, Jinliang, Masoud Rokni, and Bengt Sundén. "Simulation of fully developed laminar heat and mass transfer in fuel cell ducts with different cross-sections." *International journal of heat and mass transfer* 44.21 (2001): 4047-4058.

Appendix A

A.1 Derivations of gas concentrations across electrode from DGM

Equation A.1 shows the general form of DGM (Mason and Malinauskas [1983]).

$$\frac{\vec{N}_\alpha}{D_{K,\alpha}^{eff}} + \sum_{\beta \neq \alpha} \frac{x_\beta \vec{N}_\alpha - x_\alpha \vec{N}_\beta}{D_{\alpha,\beta}^{eff}} = -\frac{p}{RT} \cdot \frac{dx_\alpha}{dz} - \frac{x_\alpha}{RT} \cdot \left(1 + \frac{1}{D_{K,\alpha}^{eff}} \cdot \frac{B_0 p}{\mu}\right) \cdot \frac{dp}{dz} \qquad \text{(A.1)}$$

$\vec{N}_\alpha$ is the total molar flux of species α and B_0 is a constant porous-medium permeability-coefficient. z is equal to zero at the boundary between gas flow and electrode, and equal to the electrode thickness at TPB (see figure 2.1). With the assumption of constant pressure across the electrode thickness, equation A.1 can be reduced to:

$$\frac{\vec{N}_\alpha}{D_{K,\alpha}^{eff}} + \sum_{\beta \neq \alpha} \frac{x_\beta \vec{N}_\alpha - x_\alpha \vec{N}_\beta}{D_{\alpha,\beta}^{eff}} = -\frac{p}{RT} \cdot \frac{dx_\alpha}{dz}. \qquad \text{(A.2)}$$

With the assumption that the mass storage of electrode is negligible and the hydrogen oxidation is the only electrochemical reaction, total molar fluxes of different species are related to the electric current density by Faraday's law or equal to zero, for fuel side:

$$\vec{N}_\alpha = \begin{cases} \frac{j}{2F}, \alpha = \mathrm{H_2} \\ -\frac{j}{2F}, \alpha = \mathrm{H_2O} \\ 0, \alpha = \mathrm{N_2}, \mathrm{CO}, \mathrm{CO_2}\ and\ \mathrm{CH_4} \end{cases}, \qquad \text{(A.3)}$$

and for air side:

$$\vec{N}_\alpha = \begin{cases} \frac{j}{4F}, \alpha = \mathrm{O_2} \\ 0, \alpha = \mathrm{N_2} \end{cases}. \qquad \text{(A.4)}$$

After substitution of equation A.3 and A.4 into equation A.2 and transforming, the following equations can be obtained for fuel side:

$$-\frac{RT\cdot j}{2F\cdot p}\cdot\left[\left(\frac{1}{D_{K,H_2}^{eff}}+\frac{1}{D_{H_2,H_2O}^{eff}}\right)+\sum_S\left(\frac{1}{D_{H_2,S}^{eff}}-\frac{1}{D_{H_2,H_2O}^{eff}}\right)\cdot x_S\right]=\frac{dx_{H_2}}{dz}, \tag{A.5}$$

$$\frac{RT\cdot j}{2F\cdot p}\cdot\left[\left(\frac{1}{D_{K,H_2O}^{eff}}+\frac{1}{D_{H_2,H_2O}^{eff}}\right)+\sum_S\left(\frac{1}{D_{H_2O,S}^{eff}}-\frac{1}{D_{H_2,H_2O}^{eff}}\right)\cdot x_S\right]=\frac{dx_{H_2O}}{dz}, \tag{A.6}$$

$$\frac{RT\cdot j}{2F\cdot p}\cdot\left(\frac{1}{D_{H_2,S}^{eff}}-\frac{1}{D_{H_2O,S}^{eff}}\right)\cdot x_S=\frac{dx_S}{dz}, \tag{A.7}$$

where $S=\mathrm{N_2},\mathrm{CO},\mathrm{CO_2}\ and\ \mathrm{CH_4}$, and for air side:

$$-\frac{RT\cdot j}{4F\cdot p}\cdot\left(\frac{1}{D_{K,O_2}^{eff}}+\frac{1}{D_{O_2,N_2}^{eff}}\cdot x_{N_2}\right)=\frac{dx_{O_2}}{dz}, \tag{A.8}$$

$$\frac{RT\cdot j}{4F\cdot p}\cdot\frac{1}{D_{O_2,N_2}^{eff}}\cdot x_{N_2}=\frac{dx_{N_2}}{dz}. \tag{A.9}$$

Integrating equation A.7 and A.9 from boundary between gas flow and electrode to position z, change of mole fraction across electrode thickness of gas component that does not participate in electrochemical reaction can be obtained for fuel side:

$$x_S(z)=x_S(z=0)\cdot exp\left[\frac{RT\cdot j}{2F\cdot p}\cdot\left(\frac{1}{D_{H_2,S}^{eff}}-\frac{1}{D_{H_2O,S}^{eff}}\right)\cdot z\right], \tag{A.10}$$

where $S=\mathrm{N_2},\mathrm{CO},\mathrm{CO_2}\ and\ \mathrm{CH_4}$, and for air side:

$$x_{N_2}(z)=x_{N_2}(z=0)\cdot exp\left(\frac{RT\cdot j}{4F\cdot p}\cdot\frac{1}{D_{O_2,N_2}^{eff}}\cdot z\right). \tag{A.11}$$

Substituting equation A.10 into equation A.5 and A.6, and equation A.11 into equation A.8, followed by integration from boundary between gas flow and electrode to position z, change of x_{H_2}, x_{H_2O} and x_{O_2} across electrode can be obtained:

$$x_{H_2}(z) = x_{H_2}(z=0) - \frac{RT \cdot j}{2F \cdot p} \cdot \left(\frac{1}{D_{K,H_2}^{eff}} + \frac{1}{D_{H_2,H_2O}^{eff}} \right) \cdot z - \sum_S \left\{ \frac{\left(D_{H_2,H_2O}^{eff} - D_{H_2,S}^{eff} \right) \cdot D_{H_2O,S}^{eff}}{\left(D_{H_2O,S}^{eff} - D_{H_2,S}^{eff} \right) \cdot D_{H_2,H_2O}^{eff}} \cdot x_S(z=0) \cdot \left[exp\left(\frac{RT \cdot j}{2F \cdot p} \cdot \left(\frac{1}{D_{H_2,S}^{eff}} - \frac{1}{D_{H_2O,S}^{eff}} \right) \cdot z \right) - 1 \right] \right\}, \tag{A.12}$$

$$x_{H_2O}(z) = x_{H_2O}(z=0) + \frac{RT \cdot j}{2F \cdot p} \cdot \left(\frac{1}{D_{K,H_2O}^{eff}} + \frac{1}{D_{H_2,H_2O}^{eff}} \right) \cdot z + \sum_S \left\{ \frac{\left(D_{H_2,H_2O}^{eff} - D_{H_2O,S}^{eff} \right) \cdot D_{H_2,S}^{eff}}{\left(D_{H_2O,S}^{eff} - D_{H_2,S}^{eff} \right) \cdot D_{H_2,H_2O}^{eff}} \cdot x_S(z=0) \cdot \left[exp\left(\frac{RT \cdot j}{2F \cdot p} \cdot \left(\frac{1}{D_{H_2,S}^{eff}} - \frac{1}{D_{H_2O,S}^{eff}} \right) \cdot z \right) - 1 \right] \right\}, \tag{A.13}$$

where $S = \mathrm{N_2}, \mathrm{CO}, \mathrm{CO_2}\ and\ \mathrm{CH_4}$, and

$$x_{O_2}(z) = x_{O_2}(z=0) - \frac{RT \cdot j}{4F \cdot p} \cdot \frac{1}{D_{K,O_2}^{eff}} \cdot z - x_{N_2}(z=0) \cdot \left[exp\left(\frac{RT \cdot j}{4F \cdot p} \cdot \frac{1}{D_{O_2,N_2}^{eff}} \cdot z \right) - 1 \right]. \tag{A.14}$$

Similar derivations can be performed if more gas species should be considered.